

# Loss Analysis in Solar Cell

## M.Tech Project Report

Submitted in partial fulfillment of the requirements  
for the degree of

**Master of Technology  
(Microelectronics)**

by

**Rajul Jain**

**(Roll No. 17307R019)**

Under the guidance of

**Prof. Anil Kottantharayil**

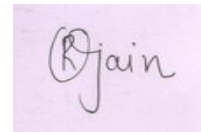


Department of Electrical Engineering  
Indian Institute of Technology Bombay  
June 2020

## Declaration

I declare that this work represents my ideas in my own words and where other ideas or words have been included, I have adequately cited and referenced proper sources. I also declare that I have adhered to all principles of academics honesty and integrity and have not falsified or misinterpreted any data/source/fact in my submission. I understand that any violation of above will be cause of disciplinary action by the institute and can also evoke the penal action from the source which have thus not been properly cited.

Date: June 30, 2020

A rectangular box containing a handwritten signature in black ink that reads "Rjain".

---

Rajul Jain  
Roll No. 17307R019  
IIT Bombay

## **Acknowledgement**

I express my gratitude to my guide Prof. Anil Kottantharayil for providing me the opportunity to work on this topic. I also express my sincerest thanks to Prof. K.L. Narasimhan and Prof. B.M. Arora for their invaluable guidance and suggestions. Also, I am grateful to IIT Bombay NCPRE baseline team and crystalline solar cell group for their continuous help during solar cell characterization and fabrication process and analysis.

Rajul Jain  
Electrical Engineering  
IIT Bombay

## Abstract

Loss analysis in electrical parameters of mono-crystalline Al-BSF large area (6"x6") silicon solar cell such as short circuit current density ( $J_{sc}$ ), open circuit voltage ( $V_{oc}$ ) and fill factor (FF) has been carried out in this study using method described in [1]. Using easy to prepare structures and commonly available characterization techniques, it is easy to extract various components of loss in different cell parameters and assess the impact of various processing steps and structures on cell performance.

Having direct correlation with device and process parameters, this analysis plays an important role in investigating exact source of performance degradation in solar cells and optimization of these parameters.

We have developed a graphical user interface using MATLAB program for quick estimation of these losses in cell.

Also, mapping of diffusion length (L) in the bulk of solar cell and surface recombination velocity (SRV) at the rear surface in solar cells has been carried out by utilizing the spectral response (SR) at different wavelengths. Different structures such as mono and multi-crystalline as well as Al-BSF and PERC have been compared based on this analysis to assess the quality of bulk and surface passivation. This comparison provides a detail understanding of exact region contributing in performance degradation of cell and necessary measures to be taken for improving this performance.

# Contents

<b>List of Figures</b>	<b>3</b>
<b>1 Introduction</b>	<b>7</b>
1.1 Solar cell and its physics . . . . .	7
1.2 Al-BSF silicon solar cell . . . . .	9
1.3 Fabrication of solar cell . . . . .	9
1.3.1 Saw Damage Removal (SDR) and texturing . . . . .	10
1.3.2 Diffusion . . . . .	10
1.3.3 PSG removal . . . . .	11
1.3.4 ARC deposition . . . . .	11
1.3.5 Edge isolation . . . . .	11
1.3.6 Metal contact printing and firing . . . . .	11
1.4 Characterization of solar cell . . . . .	12
1.4.1 Reflectance measurement . . . . .	12
1.4.2 Refractive index measurement . . . . .	12
1.4.3 Lifetime measurement . . . . .	13
1.4.4 Diffusion profile measurement . . . . .	14
1.4.5 Current-Voltage measurement . . . . .	16
1.4.6 Quantum Efficiency measurement . . . . .	16
1.4.7 Suns- $V_{oc}$ measurement . . . . .	17
1.4.8 Photo-luminescence (PL) measurement . . . . .	17
1.5 Losses in solar cell . . . . .	17
<b>2 Short Circuit Current Loss Analysis</b>	<b>20</b>
2.1 PECVD parameter optimization . . . . .	20
2.2 Methodology for Current Loss analysis . . . . .	22
2.2.1 Sunsolve simulation . . . . .	24
2.2.2 Wafer Ray Tracer simulation . . . . .	35
2.2.3 OPAL2 simulation . . . . .	40
2.3 Results and discussion . . . . .	40
2.4 Comparison of Wafer ray tracer, OPAL2 and Sunsolve . . . . .	45
<b>3 Open Circuit Voltage Loss Analysis</b>	<b>46</b>
3.1 Methodology . . . . .	46
3.1.1 Use of Suns- $V_{oc}$ for $V_{oc}$ loss analysis . . . . .	47
3.1.2 Use of Suns-PL for $V_{oc}$ loss analysis . . . . .	47
3.2 Results and discussion . . . . .	52

<b>4</b>	<b>Fill Factor Loss Analysis</b>	<b>54</b>
4.1	Methodology . . . . .	55
4.1.1	$J_{o1}$ limit of FF . . . . .	55
4.1.2	FF loss due to $R_s$ and $R_{sh}$ . . . . .	56
4.1.3	FF loss due to $J_{o2}$ . . . . .	56
4.2	Results and discussion . . . . .	56
<b>5</b>	<b>Calculation and Mapping of Diffusion Length and Back Surface Recombination Velocity</b>	<b>58</b>
5.1	Methodology . . . . .	59
5.1.1	Computation of diffusion length . . . . .	59
5.1.2	Computation of surface recombination velocity . . . . .	59
5.2	Experimental details . . . . .	59
5.3	Results and discussion . . . . .	60
<b>6</b>	<b>MATLAB program for loss analysis</b>	<b>63</b>
6.1	Details of $V_{oc}$ loss analysis tool . . . . .	63
6.2	Details of FF loss analysis tool . . . . .	65
6.3	Details of $J_{sc}$ loss analysis . . . . .	65
<b>7</b>	<b>Conclusion and Future Work</b>	<b>66</b>
7.1	Conclusion . . . . .	66
7.2	Future work . . . . .	66

# List of Figures

1.1	Working principle of solar cell [2]	7
1.2	Electrical equivalent of solar cell [3]	8
1.3	Lighted I-V curve of solar cell [3]	8
1.4	Structure of Al-BSF silicon solar cell [4]	9
1.5	Fabrication process of Solar cell	10
1.6	Solar cell basic functioning	13
1.7	a) Band to band recombination b) SRH recombination c) & d) Auger recombination	14
1.8	Emitter ECV profile	15
1.9	Emitter sheet resistance map of solar cell	15
1.10	Two diode model of solar cell	16
1.11	Measured EQE of solar cell	17
1.12	Light IV of solar cell	18
1.13	Dark IV of solar cell	18
2.1	Variation in refractive index of $SiN_x$ with wavelength for diff. $NH_3$ flow	21
2.2	Variation in refractive index of $SiN_x$ with wavelength for diff. $SiH_4$ flow	21
2.3	Variation in $SiN_x$ absorption and reflection with its thickness	22
2.4	Reflection in different structures	25
2.5	Bulk absorption in different structures	25
2.6	Output parameters for different front pyramid height	26
2.7	Output parameters for different front pyramid angle	27
2.8	Output parameters for different rear pyramid height	27
2.9	Output parameters for different rear pyramid angle	27
2.10	Variation in reflection with ARC thickness	28
2.11	Variation in bulk absorption with ARC thickness	29
2.12	Variation in transmission with ARC thickness	29
2.13	Variation in ARC absorption with ARC thickness	30
2.14	Lambertian and Phong scattering	30
2.15	Variation in reflection with Lambertian scattering fraction	31
2.16	Measured cell reflection and simulated reflection of $SiN_x+Si$ +rear reflector	32
2.17	Measured cell reflection and simulated reflection of $SiN_x+Si$ +rear reflector	33
2.18	Reflection and absorption for wafer of thickness 170 and 340 $\mu m$	34
2.19	Measured cell reflection and simulated reflection of $SiN_x+Si+Al$	35
2.20	Real refractive index for $SiN_x$	36
2.21	Imaginary refractive index for $SiN_x$	36
2.22	n and k for experiment and selected model of $SiN_x$	37
2.23	Reflection for different thickness of $SiN_x$	37
2.24	Reflection for different values of rear reflectivity	38

2.25	Reflection for different values of scattering fraction F . . . . .	38
2.26	Reflection for different values of front pyramid angle . . . . .	39
2.27	Reflection for different values of rear pyramid angle . . . . .	39
2.28	Measured cell reflection and simulated reflection from OPAL2 . . . . .	40
2.29	Reflection and absorption for rear reflectivity of 85% and 100% . . . . .	41
2.30	QE, bulk absorptance and (1- reflection) for cell . . . . .	42
2.31	Summary of $J_{sc}$ loss . . . . .	42
2.32	Reflection in $\text{SiN}_x + \text{Si} + \text{SiN}_x + \text{Al}$ for different rear pyramid height . . .	43
2.33	Absorption in $\text{SiN}_x + \text{Si} + \text{SiN}_x + \text{Al}$ for different rear pyramid height . .	44
2.34	Al absorption in $\text{SiN}_x + \text{Si} + \text{SiN}_x + \text{Al}$ for different rear pyramid height .	44
2.35	Reflection from Wafer ray tracer, OPAL2, Sunsolve and Experiment . . . .	45
3.1	Different structures fabricated for $V_{oc}$ loss analysis . . . . .	46
3.2	Different structures fabricated for $V_{oc}$ loss analysis . . . . .	47
3.3	pn product and corrected (open-short) PL count for cell . . . . .	48
3.4	Average PL count for cell, sample B and sample C . . . . .	49
3.5	Average PL count for sample C before and after edge cropping . . . . .	49
3.6	Average PL count for cell, sample B and sample C after correction . . . .	50
3.7	Measured reflection for cell, sample B and sample C . . . . .	51
3.8	$J_{sc} - iV_{oc}$ curve for cell, sample B and sample C . . . . .	51
3.9	Summary of $V_{oc}$ loss . . . . .	53
4.1	Fill factor variation with $J_{o2}$ . . . . .	54
4.2	Fill factor variation with $R_{sh}$ . . . . .	55
4.3	Summary of fill factor loss . . . . .	57
5.1	Al-BSF and PERC structures of solar cell . . . . .	60
5.2	Comparison of L values in (a) mono-crystalline (M1) and (b) multi-crystalline cells (N1), Al-BSF cells. (c) shows the histograms of the L over the wafer area. . . . .	61
5.3	Comparison of rear side SRV values in (a) mono Al-BSF (M1) and (b) mono PERC (M2). (c) shows the histograms of the SRV over the wafer area. . . . .	61
5.4	Comparison of SRV values in (a) multi Al-BSF (N1) and (b) multi PERC (N2). (c) shows the histograms of the SRV over the wafer area. . . . .	62
6.1	GUI for $V_{oc}$ loss . . . . .	63
6.2	GUI for FF loss . . . . .	65



# List of Tables

1.1	Electrical parameters of cell . . . . .	19
2.1	PECVD parameters after optimization . . . . .	22
2.2	Output parameters in $mA/cm^2$ for different surface texturing and rear reflectivity . . . . .	25
2.3	Output parameters in $mA/cm^2$ for different Lambertian fraction . . . . .	31
2.4	Output parameters in $mA/cm^2$ for $SiN_x+Si$ +rear reflector . . . . .	32
2.5	Output parameters in $mA/cm^2$ for $SiN_x+Si$ + 85 % rear reflector . . . . .	33
2.6	Output parameters in $mA/cm^2$ for different wafer thickness . . . . .	34
2.7	Input parameters in sunsolve for good fitting . . . . .	34
2.8	Output parameters in $mA/cm^2$ for $SiN_x+Si+Al$ structure . . . . .	35
2.9	Input parameters in wafer ray tracer for good fitting . . . . .	40
2.10	Output parameters in $mA/cm^2$ for structure with different rear reflectivity . . . . .	41
2.11	Summary of $J_{sc}$ loss . . . . .	43
2.12	Output parameters in $mA/cm^2$ for different rear pyramid height . . . . .	44
2.13	Output parameters in Sunsolve, Wafer ray tracer and OPAL2 (in $mA/cm^2$ ) and % difference with respect to Sunsolve . . . . .	45
3.1	Summary of $V_{oc}$ losses due to different regions in cell . . . . .	52
3.2	Summary of $V_{oc}$ loss . . . . .	53
4.1	Recombination current and resistive components for cell . . . . .	55
4.2	Summary of fill factor loss for cell . . . . .	57

# Chapter 1

## Introduction

Increasing demand of renewable and environment friendly energy source requires an efficient and feasible way of energy conversion and storage process. Solar energy is an invaluable renewable energy source which is currently gaining attention in academia as well as industry. Solar energy is finding its widespread use in almost every sector. Apart from these factors, plentiful supply of sunlight and scarcity of non-renewable energy sources in future give further motivation for uses of solar energy.

### 1.1 Solar cell and its physics

Solar cell is key component of solar energy to electrical energy conversion process and crystalline silicon is most preferred material to fabricate these cells due to more uniformity in structure and less material defects. It is a p-n junction diode which is made by contacting n and p type silicon with each other (Figure 1.1). These n-type and p-type silicon are made by doping intrinsic silicon with phosphorous and boron and called emitter and base of cell, respectively.

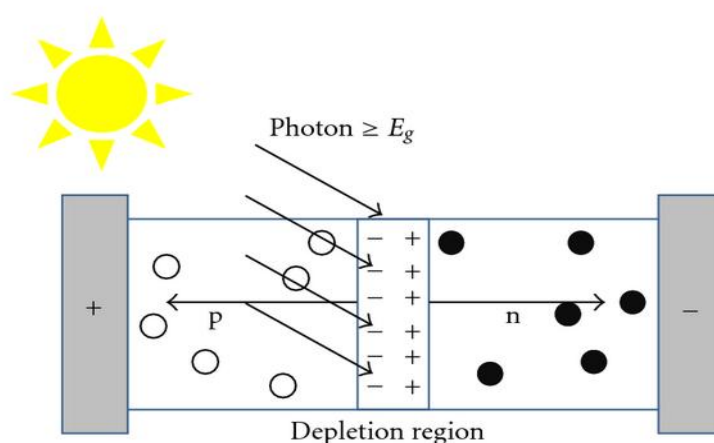


Figure 1.1: Working principle of solar cell [2]

Since n-type material has electrons as majority carriers and p-type material has holes as majority carriers, as these two materials come in contact, electrons flow from n type to p-type material and vice versa due to concentration gradient. In this process of movement,

carriers leave behind immobile ions which create an internal electric field. At steady state, flow of majority carriers due to diffusion is equal to flow of minority carriers due to electric field. Also, this region is depleted of free carriers so called depletion region. When light illuminates solar cell, incident photons with energy greater than band gap of p-n junction ( $E_g$ ) generate electron-hole pairs inside cell. These carriers move in all directions but only minority carriers are allowed to flow to other side. Depletion region helps to separate these minority carriers i.e., electrons are collected on n-side and holes are collected on p-side using contacts on both terminals of cell. This creates a potential difference between cell terminals. When a load is connected across cell, it provides current to that load. Figure 1.2 and 1.3 show electrical equivalent and lighted current-voltage (I-V) curve of solar cell, respectively.

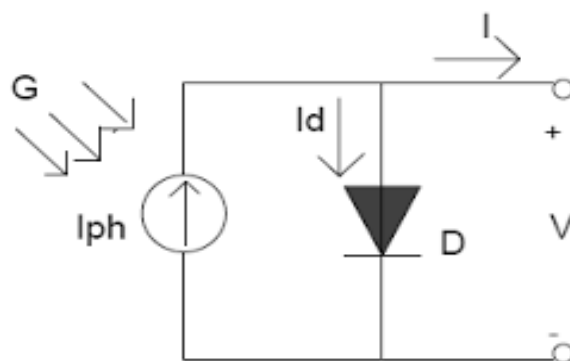


Figure 1.2: Electrical equivalent of solar cell [3]

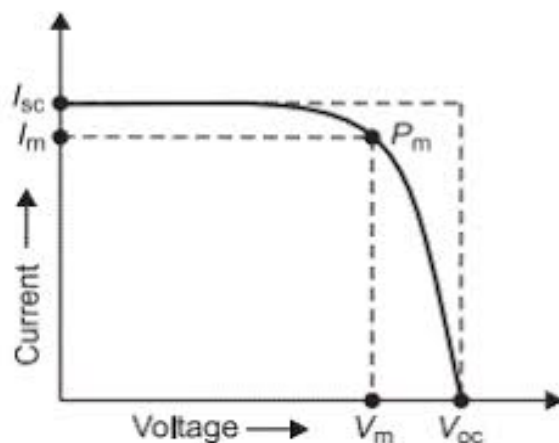


Figure 1.3: Lighted I-V curve of solar cell [3]

Equation governing current voltage relationship in solar cell is given as

$$I = I_{ph} - I_o \left[ \exp\left(\frac{V}{\eta V_t}\right) - 1 \right] \quad (1.1)$$

Where  $I_{ph}$  is current due to photons (or illuminated light),  $I_o$  is dark saturation current density of diode and tells about diode characteristics in dark such as recombination and material properties.  $V_t$  is thermal voltage and given as  $kT/q$ ;  $k$ = Boltzmann's constant,  $T$ = ambient temperature,  $q$ = electronic charge and  $\eta$  is ideality factor.

In figure 1.3,  $I_{sc}$  and  $V_{oc}$  are short circuit current (maximum achievable current) and open circuit voltage (maximum achievable voltage), respectively,  $I_m$  and  $V_m$  are current and voltage at maximum power point (at operating point). Fill factor of cell tells about maximum power provided by cell and given by ratio of area of inner rectangle and outer rectangle.

$$FF = \frac{V_m I_m}{V_{oc} I_{sc}} \quad (1.2)$$

Efficiency of solar cell is fraction of incident power that can be converted to electrical energy and given as

$$\eta = \frac{V_{oc} I_{sc} FF}{P_{in}} \quad (1.3)$$

Equation 1.3 shows that efficiency of cell is directly proportional to  $V_{oc}$ ,  $I_{sc}$  and FF. Therefore it is important to study these parameters to analyze efficiency of cell.

## 1.2 Al-BSF silicon solar cell

Figure 1.4 shows cross sectional view of standard aluminium back surface field (Al-BSF) solar cell. Solar cell without Al-BSF offers high recombination of minority carriers near rear surface of cell due to metal-semiconductor interface. To reduce this recombination, an additional layer of Al-BSF is inserted near this rear surface to reflect these minority carriers which increases their collection in bulk (provided bulk material is of good quality; bulk = base + rear). This makes structure of device from  $n^+ - p$  to  $n^+ - p - p^+$ . Front and rear contacts help in collecting a particular type of carrier from a given region.

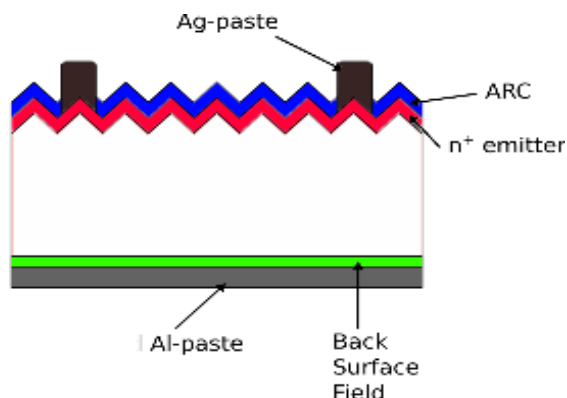


Figure 1.4: Structure of Al-BSF silicon solar cell [4]

## 1.3 Fabrication of solar cell

Fabrication of solar cells is multi-step process where each step has vital role in performance of cell. Optimization of different parameters is required to extract maximum performance from cell. Figure 1.5 describes Al-BSF silicon solar cell fabrication steps used in our baseline process.

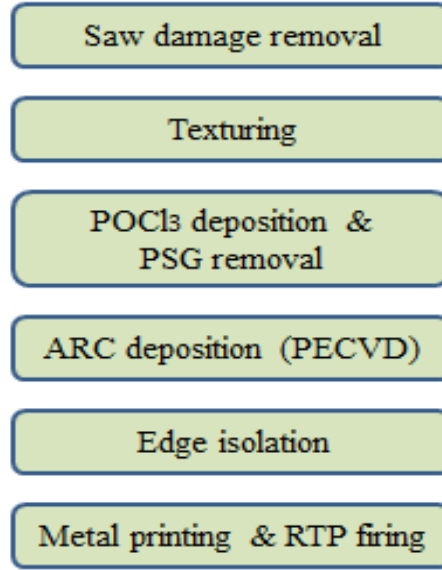


Figure 1.5: Fabrication process of Solar cell

### 1.3.1 Saw Damage Removal (SDR) and texturing

Bare wafer is obtained from ingot after diamond wire saw (DWS) process. This introduces several contamination in wafer such as defects, impurities which need to be removed from it before further processing. SDR uses a chemical (NaOCl) to clean wafer.

Also, surface of wafer needs to be modified to increase path length of light inside cell. Texturing provides this capability by introducing random pyramids (shown as zigzag structure in figure 1.4) on surface which in turn change incident angle of light to increase light trapping. For mono-crystalline wafers, alkaline texturing is done using KOH and IPA. Height and base area (square) of these pyramids must be properly chosen to obtain desired light trapping. Typical value for pyramid height and base side is 2 to 3.5  $\mu\text{m}$ . Texturing helps in reducing light reflection by trapping it inside the cell. Weighted average reflection (WAR) in cell is reduced to 10-12 % after texturing as compared to ascut wafer which has 30 % WAR.

### 1.3.2 Diffusion

After saw damage removal and texturing, wafers go under phosphorous diffusion to form  $n^+$  layer on p-type silicon. This diffusion is carried out in diffusion furnace by sending  $POCl_3$  along with  $H_2$  and  $N_2$ . Diffusion is further two step process- 1) Pre-deposition which forms layer of phosphosilicate glass (PSG) on silicon surface 2) Drive-in, in which phosphorous from PSG diffuses inside silicon. This two step diffusion process has certain process parameters such as diffusion chamber temperature, pressure and gas flow. Temperature for pre-deposition and drive-in processes is 845  $^{\circ}\text{C}$  with optimized values of pressure and gas flow which has been discussed in next chapter. Following chemical reactions describe this phenomenon of two-step diffusion process.





Phosphorous doping profile (carrier concentration vs. depth) in silicon is indicator of diffusion properties and directly impacts cell performance.

### 1.3.3 PSG removal

After phosphorous diffusion, PSG is formed on the surface of Si which acts as trap or recombination center. Typical thickness of this PSG layer is around few 100 nm. To remove this layer, HF solution with 2-4 % concentration is used.

### 1.3.4 ARC deposition

Anti-reflection coating (ARC) is used to reduce reflection from front surface of cell. When ARC layer of optimized material properties and thickness is deposited on front surface such that light rays reflected from front and rear surface of ARC and interfere destructively, overall reflection reduces to minimum. This layer is deposited usually using Plasma Enhanced chemical Vapour Deposition (PECVD) process. We are using hydrogenated silicon nitride ( $SiN_x : H$ ) as ARC in this study due to its good passivation quality for n-type emitter. Also, hydrogen atoms present in this film make bond with dangling Si atoms and reduce probability of surface recombination. Therefore, ARC acts as both reflection minimizer as well as passivator.

Thickness of ARC is given by  $t = \lambda_o/4n$  where  $\lambda_o$  = wavelength of incident light corresponding to maximum light intensity and  $n$  = refractive index of ARC material

Material properties of ARC are governed by its extinction coefficient ( $k$ ) which is related to absorption in the layer by  $\alpha = 4\pi k/ \lambda$ . This parameter imposes an upper limit on ARC thickness which can be used as increasing thickness beyond a limit may increase absorption in ARC layer itself which in turns reduces absorption in bulk of the cell. Typical average values of ARC thickness used in our baseline are 62-78  $\mu m$ .

### 1.3.5 Edge isolation

During diffusion, phosphorous is deposited on the edges of cell which causes contact between front and rear surface of cell and hence alters the desired structure of cell. To remove this phosphorous, cell edges are isolated using plasma and hence any possibility of surface contacting can be eliminated.

### 1.3.6 Metal contact printing and firing

Screen printing is most commonly used technique to form contacts on both sides of cell. Silver (Ag) is used on front while Aluminium (Al) is used on rear side. In solar cell, contacts on the front side are in form of grids to allow light to be absorbed in the cell. The screen is designed in such a way that the resistance offered by the metal contacts is minimum. At the same time, they also minimize the optical loss. For Al-BSF cells, the rear surface is fully coated with Aluminum. Metal paste with desired composition and contact properties has very important role in the printing process. These contacts have certain aspect ration (height to width ratio) which needs to be selected according to diffusion profile, contact resistance and metal shading. Therefore, it is extremely important

to use optimized metallization parameters to minimize shading, metal-semiconductor recombination and contact resistance.

After printing process, there remain residue of undesired materials in metal paste such as organic binders and paste solvents. To remove these materials and to form metal-substrate contact, samples undergo the firing process. It is multi-phase process which uses different temperatures in different phases. Firing profile (Temperature vs. Time) plays a crucial role in contact formation process. Quality of metal contacts, rear surface, bulk and front surface is affected by firing profile. It is absolutely necessary to use optimized firing parameters to obtain maximum performance of cell. Every paste manufacturer provides a certain firing profile which is required for that paste. Peak firing temperature for cells in this study is around 765 °C.

We have utilized Rapid Thermal Processing (RTP) for firing our cells using Allwin 21 AW610 instrument. It is very fast process which takes less than 10 seconds to complete the firing.

## **1.4 Characterization of solar cell**

In between different steps of fabrication, we need to characterize our structure to verify correctness of every step and to optimize process parameters. Different characterization techniques used in our baseline process are as follows.

### **1.4.1 Reflectance measurement**

This is very first characterization and has been done using Perkin Elmer Lampda 950 tool. Reflection of a sample before and after texturization are compared to assess quality of textured surface.

### **1.4.2 Refractive index measurement**

After ARC coating is deposited on wafer, it is important to measure properties such as absorption and reflection from ARC. Ellipsometer SE2000 is used to measure refractive index (shown in fig. 1.6) and thickness of film which tell about absorption and reflection properties of film. The principle behind this measurement lies in observing difference between polarization of incident and reflected light from ARC. This change is characteristic of structure and material of investigated ARC.

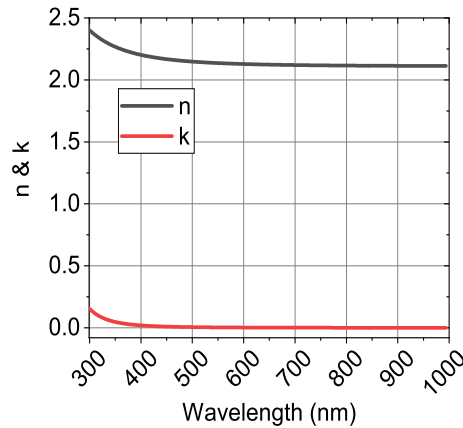


Figure 1.6: Solar cell basic functioning

### 1.4.3 Lifetime measurement

Lifetime ( $\tau$ ) of carriers in a sample tells how good the material is. It represents the time for which carriers exist before recombination. It is directly proportional to bulk diffusion length ( $L$ ) by diffusion coefficient ( $L = \sqrt{D\tau}$ ). Diffusion length is distance travelled by minority carriers before recombination. Poor lifetime deteriorates cell efficiency.

The lifetime which we are considering is effective lifetime which consists of several components depending on types of recombination in cell. Fundamentally, there are two types of recombination in a material-

1. **Radiative**- It is also known as band-to-band or direct recombination. Here, energy due to recombination of electron-hole pair is transferred to photon.
2. **Non-radiative** – This type of recombination is further divided in two types -
  - a) Trap assisted or Schokley-Read-Hall (SRH) recombination – It is defect or trap assisted recombination which is destination for electrons and holes. Energy after recombination is transferred to phonon rather than photon.
  - b) Auger recombination – Above two mechanisms of recombination needed two carriers while Auger recombination requires three carries (either 2 electrons, 1 hole or 2 holes, 1 electron). Upon recombination, extra energy is transferred either to electron to raise it high in conduction band or to hole which goes deep in valence band. Auger recombination is caused by heavy doping. In silicon solar cells, it limits the lifetime and hence efficiency of cell. Figure 1.7 [5] depicts all three recombination processes.



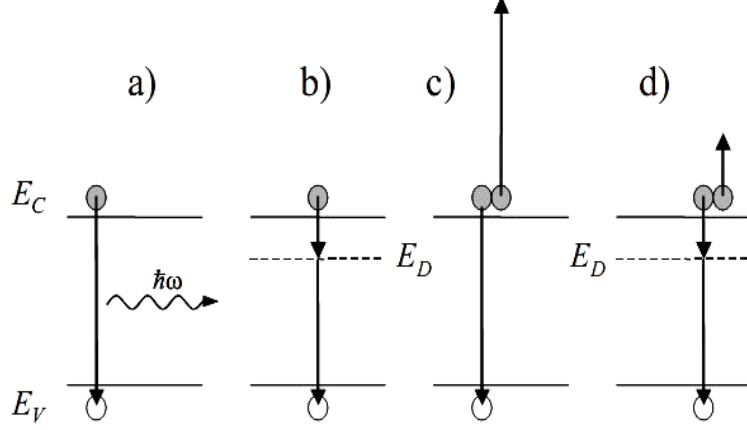


Figure 1.7: a) Band to band recombination b) SRH recombination c) & d) Auger recombination

Lifetime characterizing radiative, SRH and Auger recombination are denoted as  $\tau_{rad}$ ,  $\tau_{SRH}$ ,  $\tau_{Auger}$ , respectively. Effective lifetime is given as -

$$\frac{1}{\tau_{eff}} = \frac{1}{\tau_{rad}} + \frac{1}{\tau_{SRH}} + \frac{1}{\tau_{Auger}} \quad (1.6)$$

Effective lifetime of a sample can be estimated by measuring steady-state photo-conductance of sample at different illumination and by measuring its slope. Sinton WCT 120 lifetime tester has been used for measuring photo-conductance using a sensor which is inductively coupled to the wafer conductivity and generates an electrical signal proportional to conductivity. Complete equation and procedure to calculate emitter recombination current density  $J_{oe}$  from this lifetime data has been given in [6].

#### 1.4.4 Diffusion profile measurement

Diffusion is one of the critical steps in complete process flow of solar cell fabrication. Distribution of dopants (Phosphorous in emitter and BSF on rear surface) in sample controls its electrical properties such as sheet resistance, recombination and contact resistance. It is extremely important to control process parameters of diffusion (temperature, time, gas flow, pressure) to achieve desired properties of cell. Electrochemical capacitance voltage (ECV) measures this doping profile by measuring capacitance vs. voltage relationship and we have used WEP CVP21 ECV profiler tool to measure this profile. Figure 1.8 shows this doping profile in emitter region. Peak doping concentration and junction depth ( $N_d = N_a$ ) are two important parameters in this profile affect the performance of cell e.g., if peak doping concentration is high, contact resistance will be low which is desired feature but on the other hand, it will give rise to Auger recombination. If any of these features needs to be changed, we need to play with process parameters but very carefully. Peak Phosphorous doping concentration and junction depth are  $3 \times 10^{20} \text{cm}^{-3}$  and  $4.3 \mu\text{m}$ , respectively, for cells diffused in this study.

Another quantity which describes emitter properties is its sheet resistance which tells resistance of sheet having unity area. It has been measured using four probe system. In

this system, voltage difference is created on emitter surface using two probes and other two probes are used to measure current produces as a result of this voltage difference. Ratio of voltage and current difference provides sheet resistance. We measured sheet resistance of emitter at 49 different points on surface and its average value was found to be  $67 \Omega/\text{sq.}$  with standard deviation of  $2.39 \Omega/\text{sq.}$  To know the uniformity of sheet resistance, we also mapped it as shown in figure 1.9 which shows significant variation in sheet resistance.

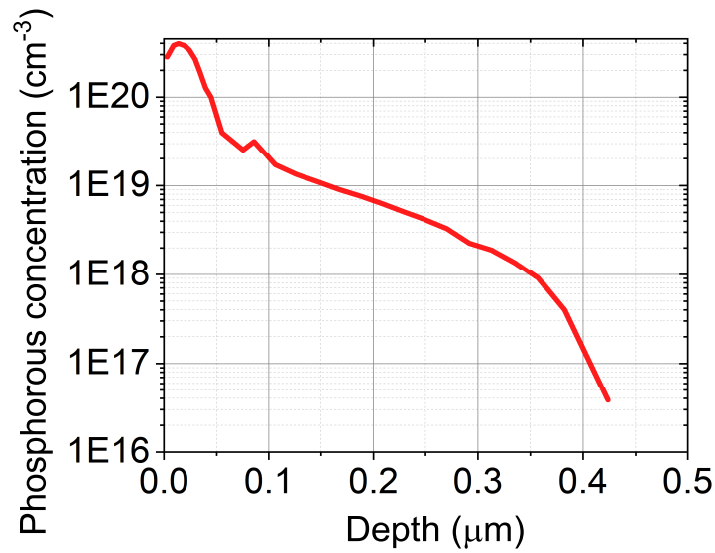


Figure 1.8: Emitter ECV profile

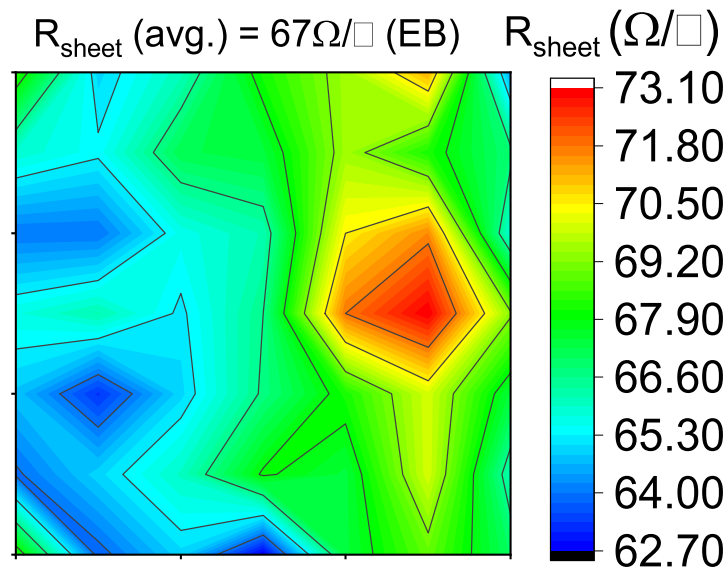


Figure 1.9: Emitter sheet resistance map of solar cell

### 1.4.5 Current-Voltage measurement

After forming metal contacts, current- voltage (dark and light) measurement is performed on this complete cell. Dark I-V curve is extremely useful source depicting recombination in several regions of the cell such as the surface, bulk and space charge region and other performance limiting factors like series and shunt resistance.

Figure 1.2 shows ideal electrical model of solar cell. Practical solar cell is accurately described by two-diode model (figure 1.10) where first diode describes recombination in bulk and near both of its surfaces and second diode tells about recombination in depletion region. Effect of series and shunt resistance is also incorporated in this model which are contributed by several processes and regions. For example, series resistance can come from emitter, bulk or contact resistance, shunt resistance can come from defect, damage or any intermediate process. All these parameters can be extracted from dark and light I-V curves of solar cell.

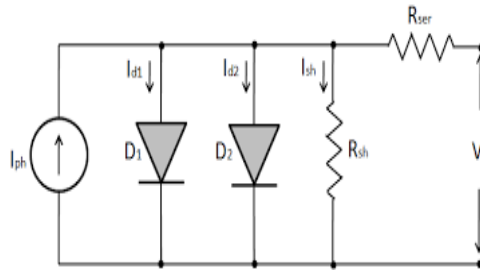


Figure 1.10: Two diode model of solar cell

Lighted I-V curve shows electrical characteristics of solar cell in presence of sunlight  $I_{sc}$  (or current density  $J_{sc} = I_{sc}/\text{Area of cell}$ ),  $V_{oc}$  and FF. This measurement is done under standard test condition (STC) i.e., 1 sun, 25 °C, AM1.5 spectrum.

### 1.4.6 Quantum Efficiency measurement

Quantum efficiency (QE) tells about efficiency with which quanta (or photons) are converted in electrons or current. It is represented as a function of wavelength and divided in two types namely external quantum efficiency (EQE) and internal quantum efficiency (IQE) and given as

$$\text{EQE} = \text{carriers collected by solar cell} / \text{incident photons on cell}$$

$$\text{IQE} = \text{carriers collected by solar cell} / \text{absorbed photons by cell}$$

Above relation shows that IQE is higher than EQE since not all incident photons are absorbed. EQE has been measured using Bentham PVE300 tool which probes the cell between two fingers. Fig. 1.11 measures measured EQE of cell. Ideally EQE should be 100 %, but there exist loss mechanisms in different regions of cell such as emitter, base, near surfaces which do not make it possible.

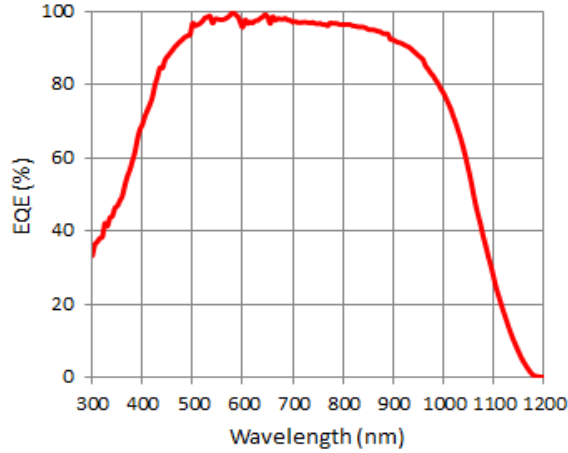


Figure 1.11: Measured EQE of solar cell

### 1.4.7 Suns- $V_{oc}$ measurement

As name implies, this technique measures  $V_{oc}$  of a sample for different light intensities or suns. Since this is done at open circuit voltage, this measurement is free from effects of series resistance. Obtained data from *suns* –  $V_{oc}$  is converted to I-V curve which is called pseudo I-V curve. By comparing pseudo I-V curve with actual I-V curve, we can estimate series resistance [7]. Additional advantage with this technique is its wide applicability on structures in intermediate process steps. Sinton WCT 120 tool has been used for performing this measurement.

### 1.4.8 Photo-luminescence (PL) measurement

This is another powerful technique which can be used to get spatial distribution of solar cell parameters such as lifetime, series resistance, recombination current etc. In this technique, cell is illuminated at certain wavelength (usually visible) which generates electron-hole pairs inside cell. Depending on dominant recombination mechanism in cell, generated carriers will recombine either radiatively or non-radiatively. Therefore, by analyzing this emitted light, information of non-radiative recombination or defects can be obtained.

We have used Greateyes LumiSolar tool for PL imaging which uses LEDs of wavelength 660 nm as light source. Also, emitted light is filtered (using high pass filter) to confine its range to silicon bandgap i.e. around 1100 nm.

## 1.5 Losses in solar cell

Ideally solar cell should convert all the incident energy to output electrical energy. However, not all generated carriers are collected from solar cell due to several loss mechanisms present. For example, some carriers will not be able to reach in bulk due to reflection, some will recombine at surface or bulk, some carriers may be absorbed in parasitic components. These losses are mainly categorized in optical, recombination and resistive losses which give rise to loss in  $J_{sc}$ ,  $V_{oc}$  and FF of cell.

Therefore, study of these losses becomes extremely useful to analyze their impact on cell

parameters and possible ways to mitigate these effects. Also, a good fundamental understanding of origin and relative contribution of each type of loss is required.

In subsequent chapters, detailed analysis of loss in  $J_{sc}$ ,  $V_{oc}$  and FF of cell will be carried out according to the method given by Johnson Wong *et. al* [1]. Each chapter has been arranged in two sections –

- A. Methodology to calculate each type of loss
- B. Results and discussion.

Electrical parameters of cell have been shown in table 1.1 along with light and dark IV curve in fig. 1.12 and 1.13, respectively.

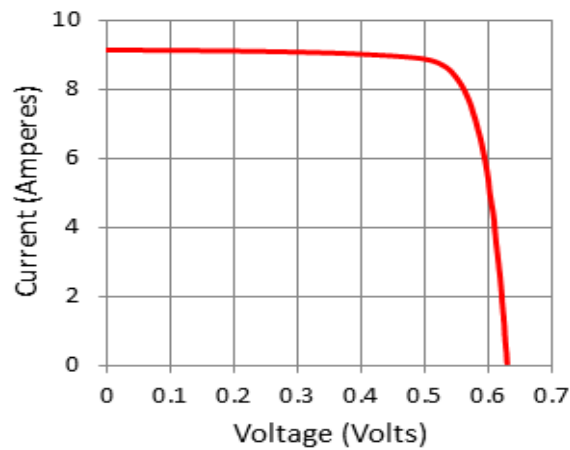


Figure 1.12: Light IV of solar cell

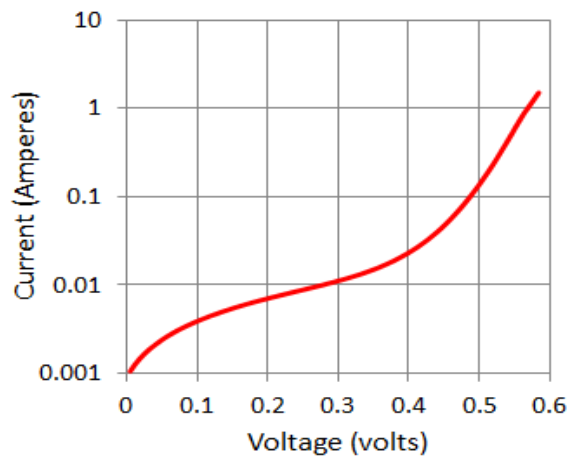


Figure 1.13: Dark IV of solar cell

Table 1.1: Electrical parameters of cell

Parameter	Value
$J_{sc}$ (mA/cm <sup>2</sup> )	37.36
$V_{oc}$ (mV)	628.7
$J_{mpp}$ (mA/cm <sup>2</sup> )	35.03
$V_{mpp}$ (mV)	537.43
FF (%)	80.2
$\eta$ (%)	18.8
$R_s$ (m $\Omega$ - cm <sup>2</sup> )	280
$R_{sh}$ (k $\Omega$ - cm <sup>2</sup> )	8.1

## Chapter 2

# Short Circuit Current Loss Analysis

Current loss in solar cell depends on optical properties such as reflection and absorption as well as on recombination. These losses can happen in any region of cell like front metal grid, anti-reflection coating (ARC), emitter, base and rear.

Based on contribution in current loss from different regions in cell, we can divide it in 6 types. 1) ARC reflection 2) Escape reflection 3) ARC absorption 4) Front metal shading 5) Poor bulk collection loss 6) Parasitic absorption in rear of cell

We deposited  $\text{SiN}_x$  as ARC by varying different process parameters in PECVD and analyzed its impact on  $\text{SiN}_x$  properties and hence on current loss in this film.

In this chapter, we have addresses these two problems one by one. Section 2.1 describes PECVD process optimization and section 2.2 mentions different current loss components in cell.

### 2.1 PECVD parameter optimization

PECVD has been used to deposit  $\text{SiN}_x$  on top of Si wafer. It uses certain gases ( $\text{NH}_3$ ,  $\text{SiH}_4$  and  $\text{N}_2$ ) and plasma to deposit this layer. Thickness, refractive index and uniformity of this layer depend on different process parameters such as chamber pressure, temperature, gas flow, time and RF power which in turn affect current absorption or loss due to this layer. Therefore, it is important to analyze this dependency and use optimized process parameters to minimize the current loss. All samples have gone through RTP firing.

Figure 2.1 and 2.2 show refractive index and thickness for different flow (in sccm) of  $\text{NH}_3$  and  $\text{SiH}_4$ , respectively.

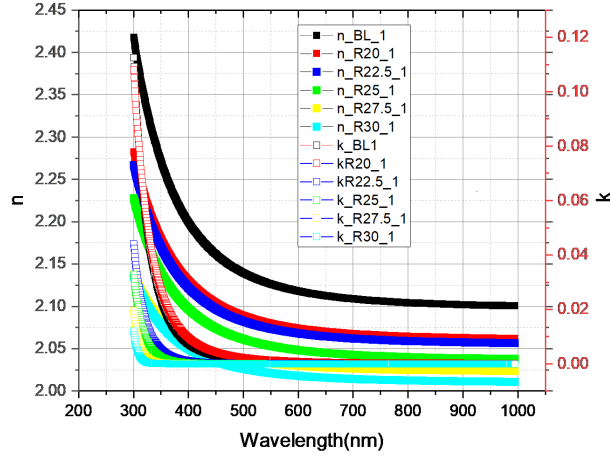


Figure 2.1: Variation in refractive index of  $SiN_x$  with wavelength for diff.  $NH_3$  flow

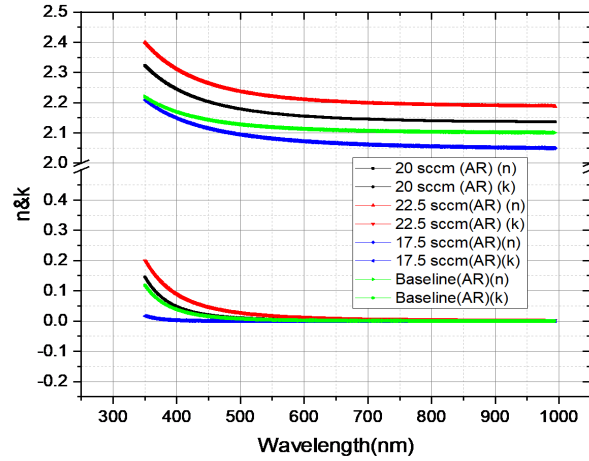


Figure 2.2: Variation in refractive index of  $SiN_x$  with wavelength for diff.  $SiH_4$  flow

From these figures it is clear that  $NH_3$  flow of 30 sccm and  $SiH_4$  flow of 17.5 sccm give lower value of imaginary refractive index (k) which is responsible for light absorption in this layer. Here BL stands for baseline process which is standard but not optimized and digit 1 indicates point on center of wafer.

Chamber pressure impacts uniformity of thickness for deposited layer. We checked the uniformity for different chamber pressures and selected the pressure which gives more uniformity. Similarly process time affects  $SiN_x$  thickness uniformity and refractive index. A proper values of process time has been chosen which provides desired values of n & k as well as better thickness uniformity.

Table 2.1 summarizes all optimized process parameters that we have used for  $SiN_x$  deposition.



Table 2.1: PECVD parameters after optimization

Parameter	Value
Chamber pressure	1100 mTorr
Chamber temperature	380 °C
RF power	20 W
Deposition time	333 sec
NH <sub>3</sub> flow	30 sccm
SiH <sub>4</sub> flow	17.5 sccm
N <sub>2</sub> flow	980 sccm

We used OPAL2 simulation tool [8] to find reflection and absorption in SiN<sub>x</sub> layer using refractive index and thickness obtained after optimization. We plotted spectral reflection, weighted average reflection and absorption and current due to these components for different SiN<sub>x</sub> thickness as shown in figure 2.3. It shows an optimum value of SiN<sub>x</sub> thickness for minimum absorption and reflection which in turn can be obtained by using appropriate process parameters.

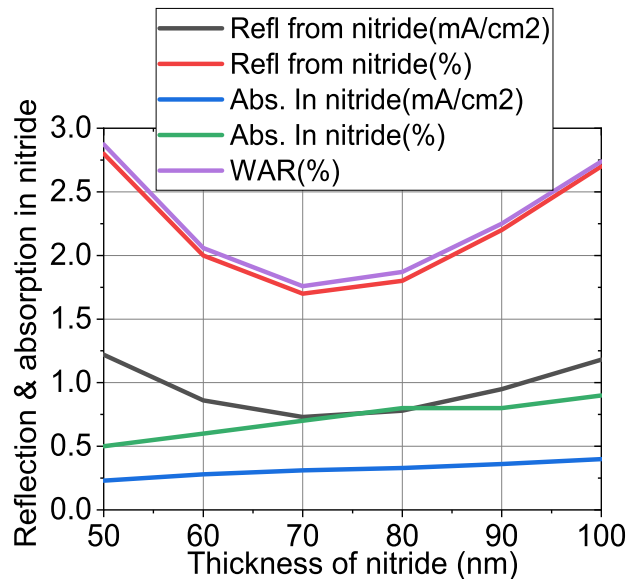


Figure 2.3: Variation in SiN<sub>x</sub> absorption and reflection with its thickness

## 2.2 Methodology for Current Loss analysis

Difference of EQE from ideal case (100%) in a solar cell indicates about lost current. By measuring this difference and finding different components of this difference, we can quantify each type of loss in cell.

It is easy to find current loss due to front metal shading caused by fingers and busbars. The geometry of fingers and busbars governs this loss hence by measuring the area of all fingers and busbars and dividing it by cell area, metal fraction and hence metal shading loss can be calculated. However, easier way to calculate it is to find the short circuit current density  $J_{sc}$  from 1-sun I-V measurement and subtracting it from current density

obtained by integrating EQE since latter measurement is done by probing cell front surface between the fingers.

$$J_{sc} \text{ loss due to metal shading} = J_{sc} \text{ from EQE} - J_{sc} \text{ from IV}$$

Although total reflection from cell can be measured experimentally, we need simulation techniques to get ARC and escape reflection separately. Similarly to find parasitic absorption in rear part of cell and bulk collection loss, we need its bulk absorptance since absorptance tells about maximum light absorption in absence of any recombination. Absorption in front  $SiN_x$  or ARC also needs simulation of cell structure.

Therefore, we decided to use simulation to find different current losses in cell. These simulation techniques offer a very powerful way to analyse the losses in cell. They offer several advantages over experimental processes such as easy analysis and less time consumption. We analyzed different simulation tools available on PV lighthouse [8] and selected best possible tool for our analysis. A brief description of different simulation tools is given as follows.

### 1. OPAL2

- It analyzes properties of thin film to calculate reflection, absorption and transmission from film.
- It is possible to insert custom material in this tool.
- It does not consider rear surface morphology hence does not give accurate results for long wavelength range.

### 2. Wafer Ray Tracer

- It incorporates the effect of the wafer bulk and both of its surfaces and permits the assessment of all optical losses and light trapping.
- No option for inserting custom material (ARC or other)
- More computationally intensive than OPAL2.

### 3. Sunsolve

- It determines the optical and electrical performance of solar cell by using ray tracing & thin-film optics and equivalent circuits, respectively.
- Custom material can be easily added.
- It considers surface morphology on both sides of cell.
- Built-in structures of PERC cell, Bi-facial cell, hetero-junction cell are available in this tool which are helpful for quick estimation of losses and comparison of output parameters.

Our main objective was to simulate a structure which depicts our cell. Therefore, it was required to use a structure whose reflection matches with measured cell reflection spectrally with a good accuracy. We selected reflection because this is the only common parameter in simulation and measurement.

All these tools need some input parameters characterizing solar cell such as wafer and ARC thickness, surface morphology, rear layer thickness and reflectivity. Use of appropriate values for these parameters is crucial to get accurate results from simulation.

## 2.2.1 Sunsolve simulation

We applied several iterations on input parameters to obtain a set of parameters whose reflection matches with cell measured reflection. We started from surface texturing and reflection at rear.

### A. Surface texturing and rear reflector

Surface texturing is used to reduce reflection in solar cell by bouncing back the reflected light into bulk of cell. To obtain surface texturing, surface of the cell is etched along the faces of the crystal planes to grow random upright pyramids on the surface of cell (while doing experiment). First, we analyzed difference of texturing on single and both surfaces of cell.

Our cell has Al-BSF, Al-Si alloy and Al at rear but due to unavailability of refractive index data of these rear layers, we could not insert these layers in simulation. Therefore, it was necessary to use a layer which stops light from going out from rear surface. We can take either rear reflector or any layer which absorbs remaining light left after absorption in cell and reduces transmission to almost zero value. In this subsection, we have used rear reflector. Later, we will see the effect of taking rear absorbing layer instead of reflector.

Four structures of different combinations of texturing and reflectivity have been simulated.

#### Structures -

1.  $\text{SiN}_x$ + Si+ Both side texturing+ No rear reflector
2.  $\text{SiN}_x$ + Si+ Both side texturing+ 100% rear reflector
3.  $\text{SiN}_x$ + Si+ Front side texturing+ No rear reflector
4.  $\text{SiN}_x$ + Si+ Front side texturing+ 100% rear reflector

#### Input parameters -

- Random upright pyramid with angle =  $54.74^\circ$  and height =  $2.8 \mu\text{m}$
- $\text{SiN}_x$  thickness (custom baseline data) = 63 nm
- Si wafer thickness =  $180 \mu\text{m}$ .
- We considered no light scattering

Reflection of these four structures was compared with measured reflection of cell as shown in fig. 2.4 & 2.5 and corresponding results in table 2.2.

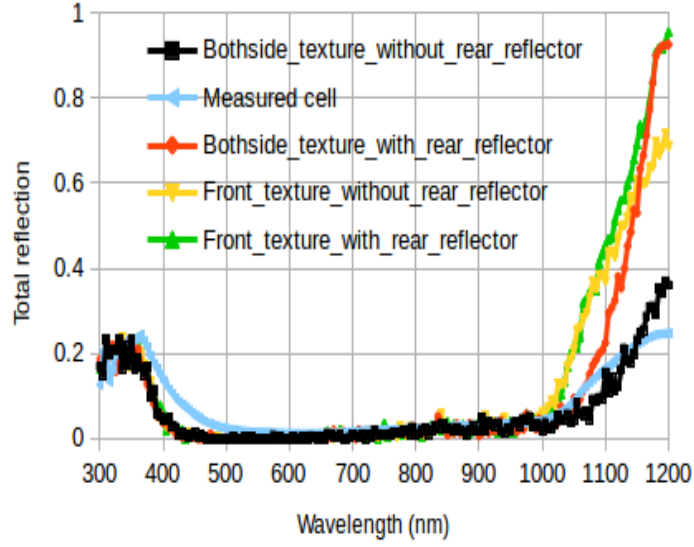


Figure 2.4: Reflection in different structures

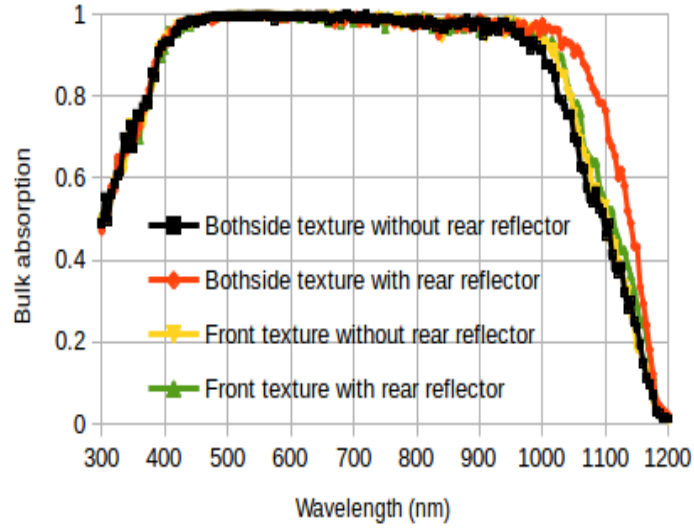


Figure 2.5: Bulk absorption in different structures

Table 2.2: Output parameters in  $mA/cm^2$  for different surface texturing and rear reflectivity

Structure	ARC refl.	Escape refl.	Bulk abs.	ARC abs.	Transmission
1	0.95	0.73	41.39	0.29	2.95
2	0.94	2.13	42.85	0.34	0
3	0.94	2.57	41.72	0.29	0.79
4	0.99	2.96	42.01	0.32	0

**Observation** - Fig. 2.4 shows that deviation from desired reflection is less without rear reflector and both side texturing. However, in the absence of rear reflector, a significant amount of light will transmit from rear surface. Therefore, we preferred the case which considers rear reflector and hence depicts our cell structure more accurately.

In presence of rear reflector, both side texturing gives less light reflection which is due to improved light confinement. We need to adjust parameters of surface morphology (pyramids) and rear reflector such that we get reflection closer to measured cell reflection.

## B. Pyramid height and angle

Surface texturing introduces pyramids which are mainly random upright in nature for our cell. These pyramids have certain height, width and characteristic angle defining their shape and are very effective in confining light into the cell.

We analysed variation in output parameters (in terms of current) with front and rear surface pyramid angle  $\omega$  and height  $H$  to select a reasonable values of these inputs (fig. 2.6 - 2.9). We have changed only one parameter at a time taking default value for other input parameters which are  $54.74^\circ$  for pyramid angle and  $3.54 \mu\text{m}$  for pyramid height.  
**Structure** -  $\text{SiN}_x + \text{Si}$ , no rear layer or reflector

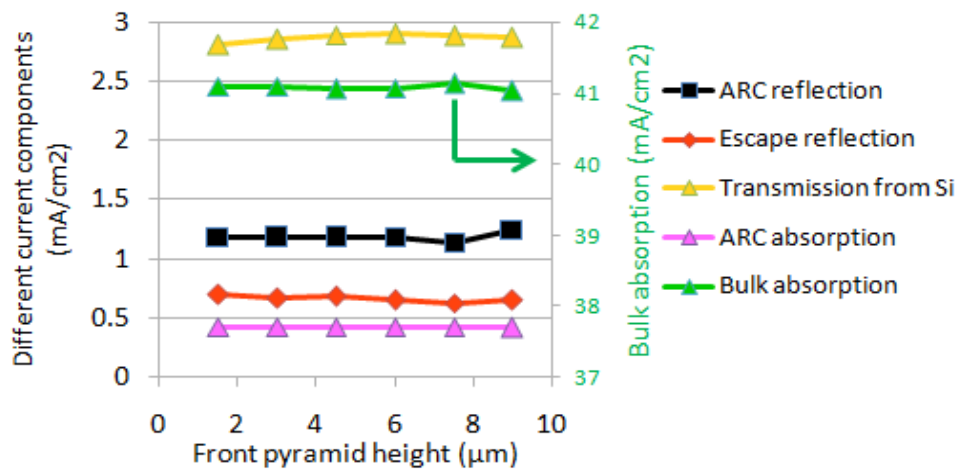


Figure 2.6: Output parameters for different front pyramid height

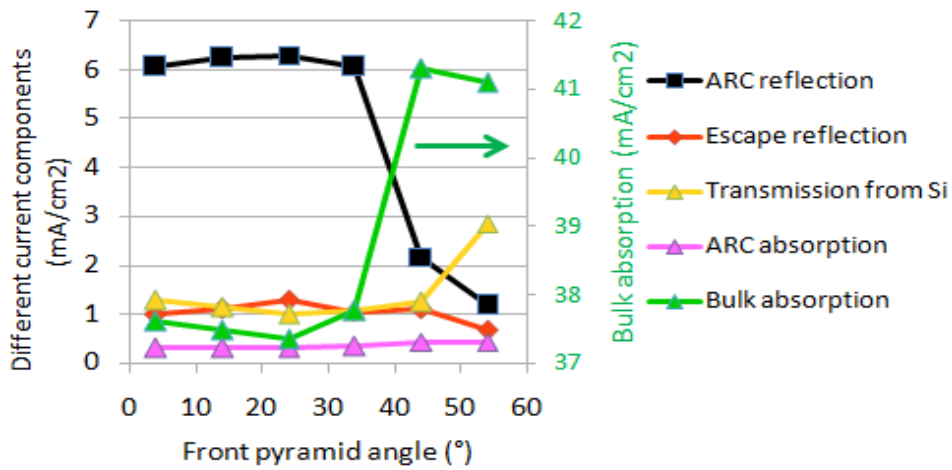


Figure 2.7: Output parameters for different front pyramid angle

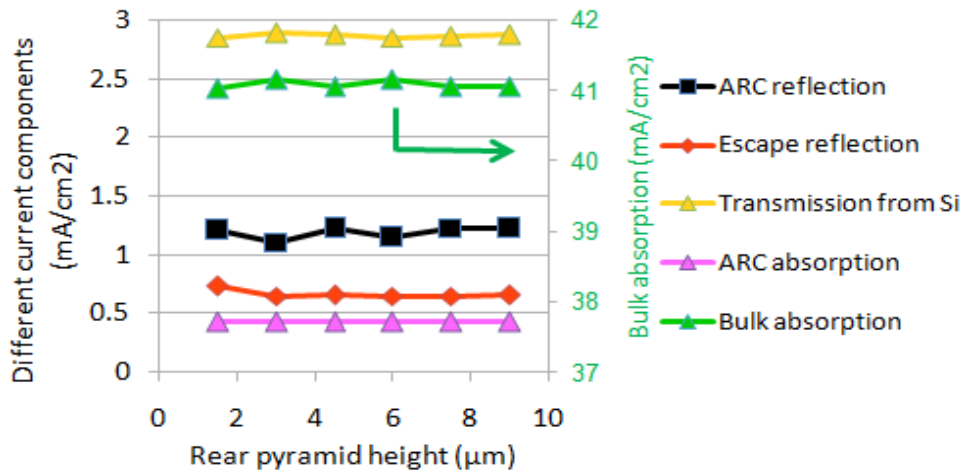


Figure 2.8: Output parameters for different rear pyramid height

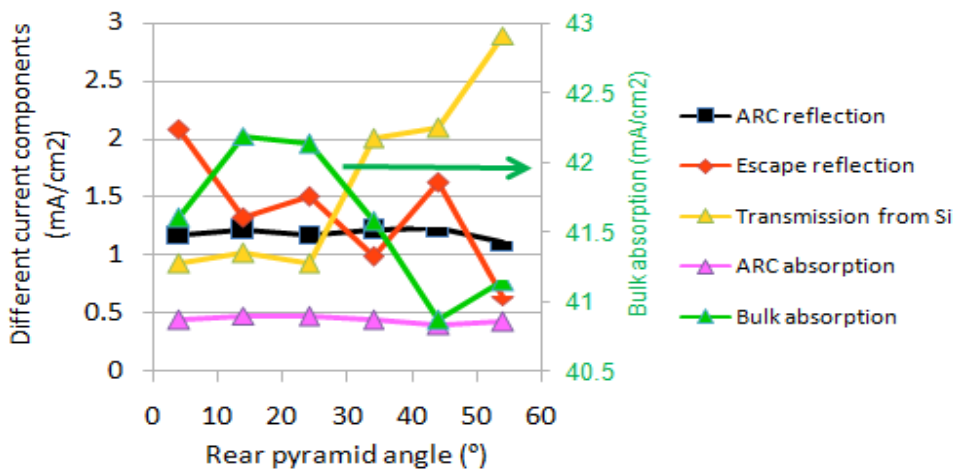


Figure 2.9: Output parameters for different rear pyramid angle

**Observation** Fig 2.6 and 2.8 show that output parameters are very less sensitive to variation in front or rear surface pyramid height.

It is clearly visible from fig. 2.7 that as front pyramid angle increases beyond  $32^\circ$ , ARC reflection starts to drop significantly and hence bulk absorption starts to increase. Transmission from rear surface to outside increases for pyramid angle larger than  $43^\circ$  but this increment is smaller than that in bulk absorption. Therefore, it may be the indication of improved light confinement at these pyramid angles.

Rear pyramid angle has comparatively less effect on output. For example, escape reflection decreases for angle in  $0-12^\circ$  range and after this it suddenly starts to increase and this behaviour continues. Bulk absorption varies accordingly.

Results indicate that, pyramid angle affect the results significantly and hence, need to be investigated further.

### C. ARC thickness

As we have seen earlier that reflection in short wavelength (300-500 nm) is governed by ARC thickness (and refractive index), it is important to use a right value of ARC thickness. We analyzed impact of ARC thickness on output.

**Structure** -  $\text{SiN}_x$ +Si with planar wafer on both sides having thickness of  $180 \mu\text{m}$ .

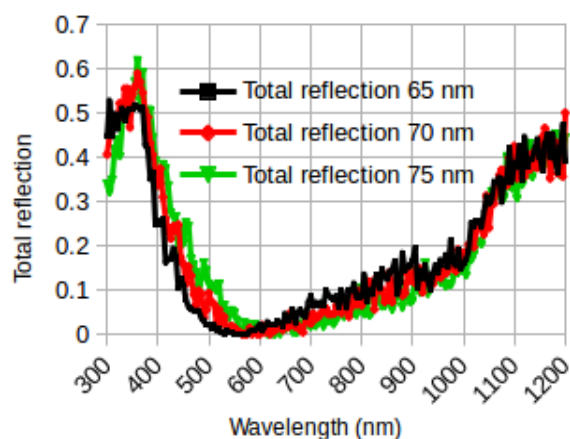


Figure 2.10: Variation in reflection with ARC thickness

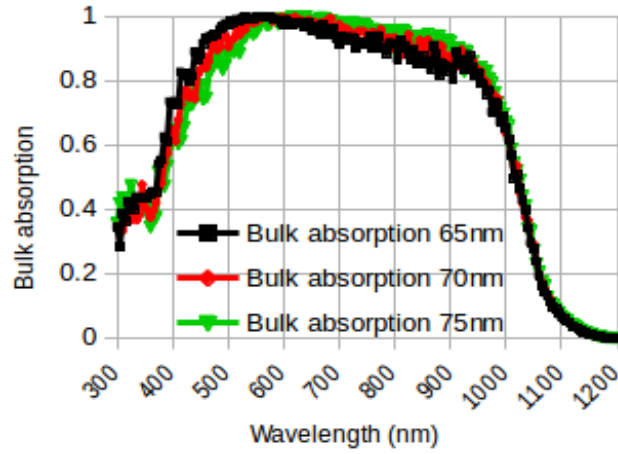


Figure 2.11: Variation in bulk absorption with ARC thickness

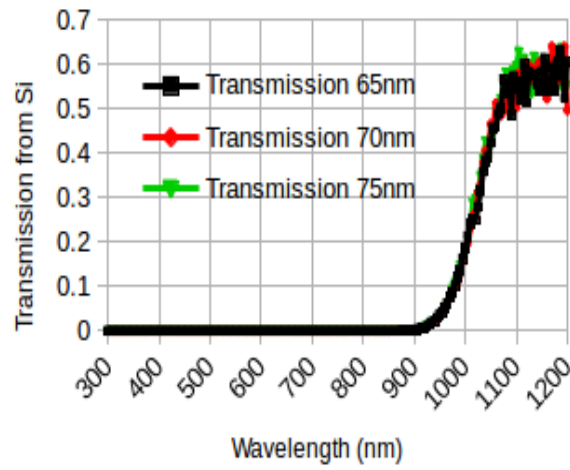


Figure 2.12: Variation in transmission with ARC thickness



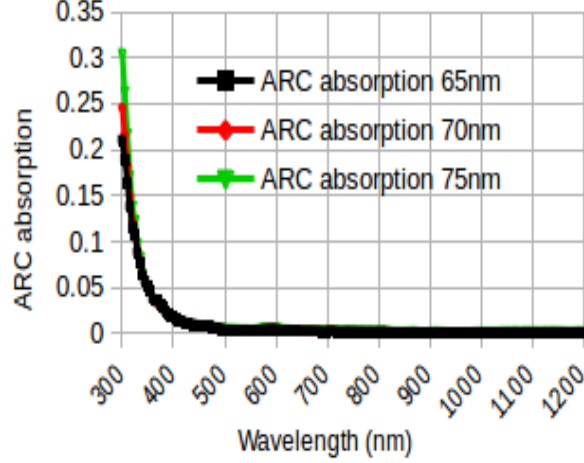


Figure 2.13: Variation in ARC absorption with ARC thickness

**Observation** - From fig. 2.10 and 2.11, it is clear that as ARC thickness is increased, reflection minima (and bulk absorption maxima) shifts to higher wavelength side. No considerable difference is observed in transmission (fig. 2.12) and ARC absorption increases slightly (fig. 2.13).

#### D. Light scattering

Some researchers have mentioned that surfaces with random upright pyramids have considerable light scattering. Therefore, light scattering should be taken into account while modelling random upright pyramids to get accurate results from simulation. There are two types of scattering - 1) Lambertian scattering and 2) Phong scattering both of which have been described here [8].

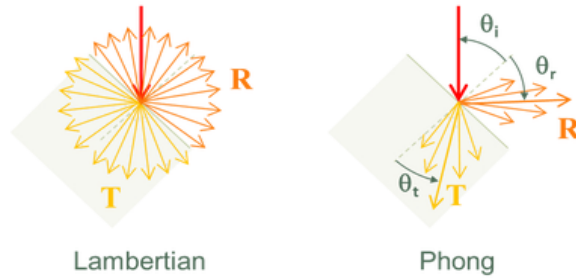


Figure 2.14: Lambertian and Phong scattering

**D.1 Lambertian scattering** - with Lambertian scattering, the spherical polar angles that define the ray's new direction are determined stochastically from  $\theta = \arccos(\chi^{0.5})$  and  $\phi = 2\pi\chi$  where  $\chi$  is a random number,  $0 \leq \chi < 1$ .

We included Lambertian scattering for pyramids on both sides and no rear reflector was taken. Other input parameters are same as mentioned earlier. For different amount of Lambertian scattering fraction, we plotted total reflection and compared with measured reflection of cell.

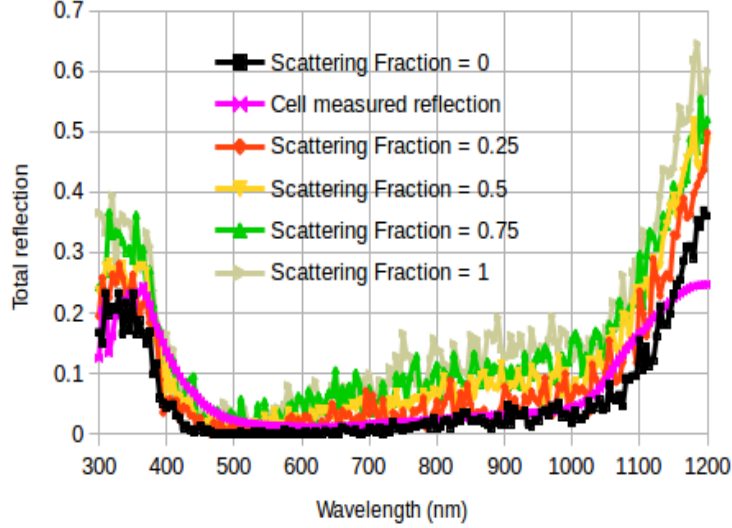


Figure 2.15: Variation in reflection with Lambertian scattering fraction

Table 2.3: Output parameters in  $mA/cm^2$  for different Lambertian fraction

Lambertian fraction	ARC refl.	Escape refl.	Bulk abs.	ARC abs.	Transmission
0	0.95	0.73	41.39	0.29	2.95
0.25	1.94	0.95	40.74	0.29	2.35
0.5	2.82	1.11	40.22	0.29	1.87
0.75	3.8	1.18	39.43	0.3	1.55
1	4.53	1.36	38.92	0.3	1.16

**Observation** - fig. 2.15 shows that as scattering fraction is increased in absence of rear reflector, reflection in our structure also increases and deviates more from measured cell reflection. Therefore, we need to iterate parameters of scattering model to obtain best possible fit.

**D.2 Phong scattering** - for case of Phong scattering, angles are given as  $\Delta\theta = \arccos(\chi^{\frac{1}{\alpha+1}})$  and  $\phi = 2\pi\chi$  where  $\alpha$  is called the Phong exponent and  $\Delta\theta$  is the difference between the new angle and the specular reflection. Phong scattering is identical to Lambertian scattering when  $\alpha = 1$  and  $\theta_i = 0$  (normal incidence) and it is identical to 'no scattering' when  $\alpha$  is infinite.

Phong scattering represents surface of random upright pyramids more accurately [9] so we decided to include this scattering in simulation.

We used rear reflector with  $SiN_x+Si$  structure considering Phong scattering. Again, two cases were taken, one with only front texturing and second with both side texturing.

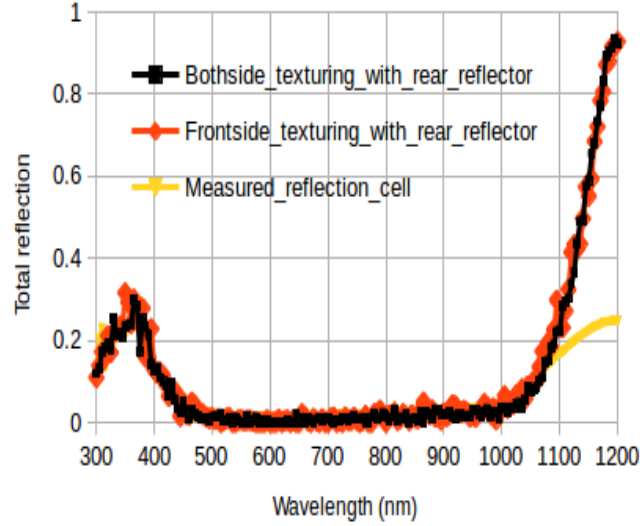


Figure 2.16: Measured cell reflection and simulated reflection of  $\text{SiN}_x+\text{Si}+\text{rear reflector}$

Table 2.4: Output parameters in  $\text{mA}/\text{cm}^2$  for  $\text{SiN}_x+\text{Si}+\text{rear reflector}$

Structure	ARC refl.	Escape refl.	Bulk abs.	ARC abs.	transmission
Both side texture	1.1	2.13	42.65	0.38	0
Front side texture	1.2	2.18	42.51	0.38	0

**Observation** - Fig. 2.16 and table 2.4 show that with Phong scattering, there is not significant difference in output with both side and only front side texturing -this verifies better light confinement property of Phong scattering. Also we need to reduce rear reflectivity to get a good fitting with measured data.

### E. Rear reflectivity

We adjusted rear reflectivity and found that 85% reflectivity at rear gives a good matching as shown in fig. 2.17. This includes effect of Phong scattering.

#### Input parameters -

- Front pyramids (random upright) –  $48^\circ$ ,  $5 \mu\text{m}$
- Rear pyramids (random upright) –  $51^\circ$ ,  $5 \mu\text{m}$
- $\text{SiN}_x$  thickness – 75 nm
- Wafer thickness –  $170 \mu\text{m}$
- Phong exponent  $\alpha = 20$  and scattering fraction = 1

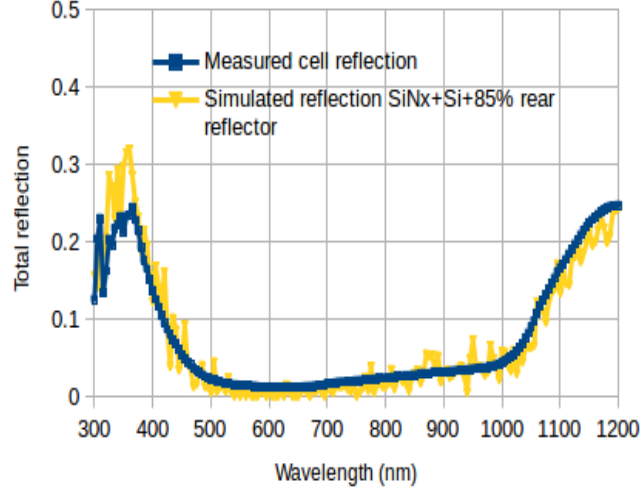


Figure 2.17: Measured cell reflection and simulated reflection of  $\text{SiN}_x+\text{Si}+\text{rear reflector}$

Table 2.5: Output parameters in  $\text{mA}/\text{cm}^2$  for  $\text{SiN}_x+\text{Si}+ 85\%$  rear reflector

Parameter	ARC refl.	Escape refl.	Bulk abs.	ARC abs.	Rear abs.
Value	1.5	0.62	40.61	0.29	3.24

**Observation** -From fig. 2.17, we see that with Phong scattering and above mentioned input parameters, we are able to obtain simulation results which are in good agreement with measured reflection. Therefore, bulk absorptance and other output parameters of this structure has been used for current loss calculation as will be mentioned in Results and Discussion section.

## F. Wafer thickness

We used two values of wafer thickness (only for simulation) and analyzed its impact on results (fig. 2.18) considering Phong scattering.

### Input parameters -

- Front pyramids (random upright) –  $48^\circ$ ,  $5\ \mu\text{m}$
- Rear pyramids (random upright) –  $51^\circ$ ,  $5\ \mu\text{m}$
- $\text{SiN}_x$  thickness –  $75\ \text{nm}$
- 100% reflector at rear

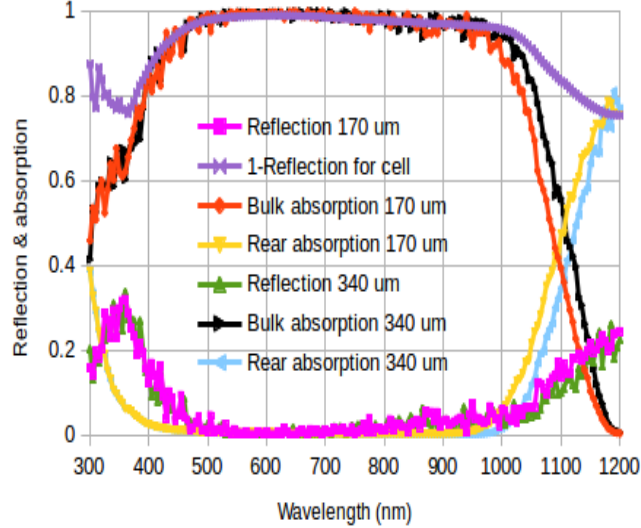


Figure 2.18: Reflection and absorption for wafer of thickness 170 and 340  $\mu\text{m}$

Table 2.6: Output parameters in  $\text{mA}/\text{cm}^2$  for different wafer thickness

Wafer thickness	ARC refl.	Escape refl.	Bulk abs.	ARC abs.	transmission
170 $\mu\text{m}$	1.5	0.62	40.61	0.29	3.24
340 $\mu\text{m}$	1.47	0.48	41.51	0.28	2.56

**Observation** – from fig. 2.18 we can see that increasing wafer thickness improves light trapping capability of bulk hence bulk absorption increases. However, this reduces difference between (1-reflection) for cell and bulk absorptance which indicates that we can not take this difference as measure of rear parasitic loss because this loss should not change with wafer thickness. To correctly calculate parasitic loss, we need to compare structure with ideal (100% rear reflectivity or maximum bulk absorption) and practical scenario (finite rear reflectivity).

From above analysis, we reached at a set of input parameters in sunsolve which is best suitable for this study as shown in table 2.7.

Table 2.7: Input parameters in sunsolve for good fitting

Input parameter	Value
SiN <sub>x</sub> thickness	75 nm
Wafer thickness	170 $\mu\text{m}$
Rear reflectivity	85 %
Phong scattering fraction	1
Phong exponent	20
Front pyramid angle	48°
Front pyramid height	5 $\mu\text{m}$
Rear pyramid angle	51°
Rear pyramid height	5 $\mu\text{m}$

## G. SiN<sub>x</sub>+Si+Al structure for fitting

Since fitting is very good when we considered Phong scattering, we also tried to take rear absorbing layer and iterated parameters of SiN<sub>x</sub>+Si+Al structure to achieve best possible fit by considering Phong scattering and procedure mentioned in [9]. Fig. 2.19 compares simulated and measured reflection.

### Input parameters -

- Thickness of rear Al and SiN<sub>x</sub> – 10 μm and 75 nm, respectively
- Front pyramids (random upright) -  $\omega = 48^\circ$ , H = 5 μm
- Rear pyramids (random upright) -  $\omega = 51^\circ$ , H = 3 μm
- Phong exponent -  $\alpha = 20$  and scattering fraction = 1 for both surfaces

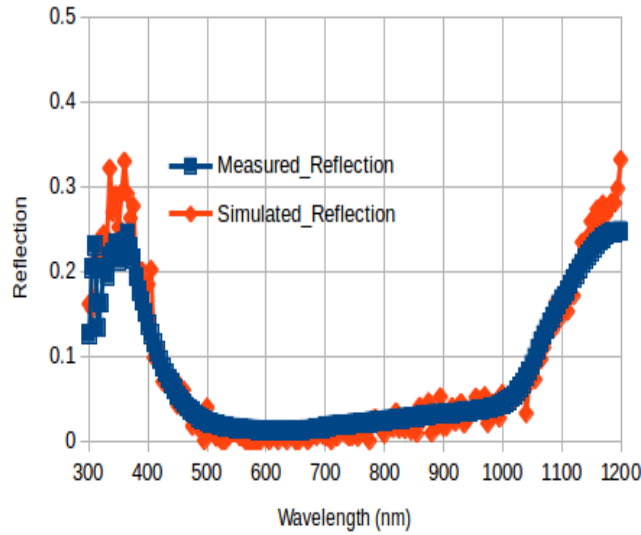


Figure 2.19: Measured cell reflection and simulated reflection of SiN<sub>x</sub>+Si+Al

Table 2.8: Output parameters in  $mA/cm^2$  for SiN<sub>x</sub>+Si+Al structure

Parameter	ARC refl.	Escape refl.	Bulk abs.	ARC abs.	Al abs.	Transmission
Jsc	1.47	0.77	40.87	0.29	2.88	0

**Observation** - Since the fitting in fig. 2.19 looks reasonable, we can use output parameters of this structure also to estimate current losses similar to SiN<sub>x</sub>+Si+rear reflector structure.

## 2.2.2 Wafer Ray Tracer simulation

As mentioned earlier that it is not possible to insert custom data in wafer ray tracer. However, we can try to select input parameters in wafer ray tracer such that we are able

to get fit for measured reflection as closer as possible (if not very accurate). We changed one parameter at a time keeping other parameters constant.

First we selected model of  $\text{SiN}_x$  among available models in refractive index library of wafer ray tracer. We selected a model by comparing its refractive index with experimentally measured reflection (fig. 2.20, 2.21 and 2.22).

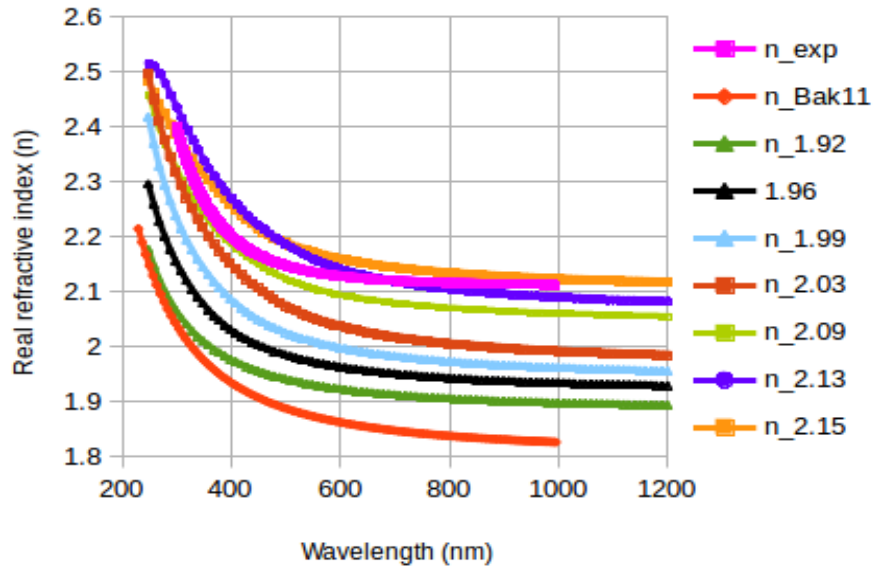


Figure 2.20: Real refractive index for  $\text{SiN}_x$

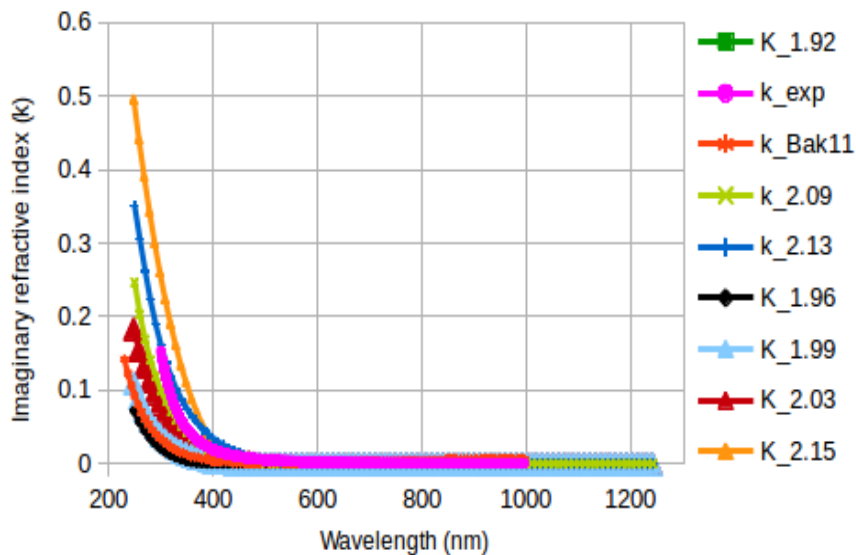


Figure 2.21: Imaginary refractive index for  $\text{SiN}_x$

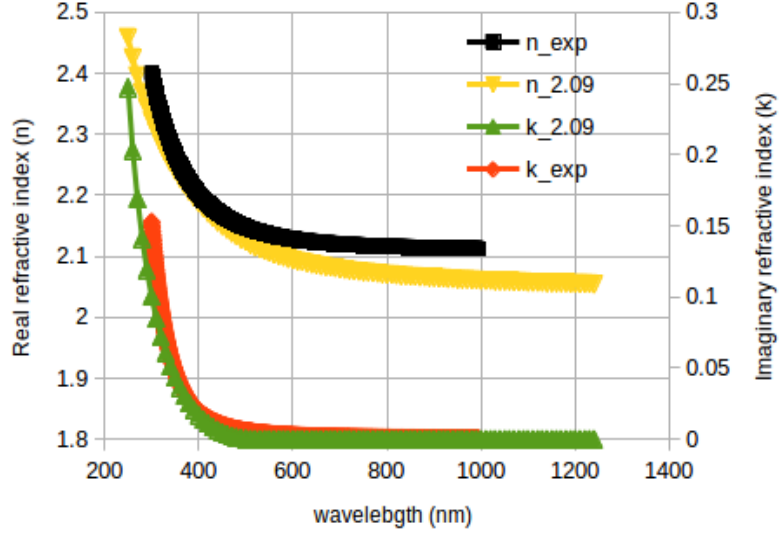


Figure 2.22:  $n$  and  $k$  for experiment and selected model of  $\text{SiN}_x$

From these figures, it is clear that the model PECVD 2.09(Vog15) of  $\text{SiN}_x$  gives both  $n$  and  $k$  close to experimental data. Therefore, we selected this nitride for further analysis. Then we checked the thickness of  $\text{SiN}_x$  for good fitting in short wavelength range as shown in fig. 2.23. It shows thickness of 75 nm is appropriate for our use.

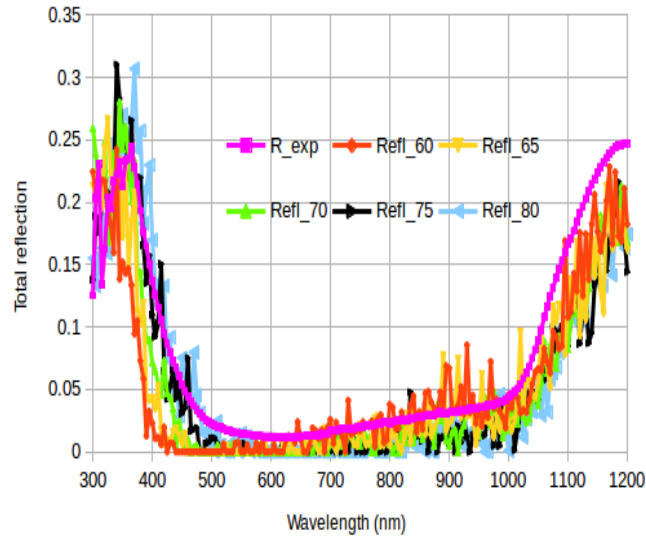


Figure 2.23: Reflection for different thickness of  $\text{SiN}_x$

Similar to sunsolve, we wanted to simulate structure  $\text{SiN}_x + \text{Si} + \text{real reflector}$  in wafer ray tracer also. Therefore, next step was to select reflectivity of rear reflector and scattering fraction for surface pyramids. Both of these have been shown in fig 2.24 and 2.25. We can see that rear reflectivity of 0.9 and scattering fraction of 0 are good choice.



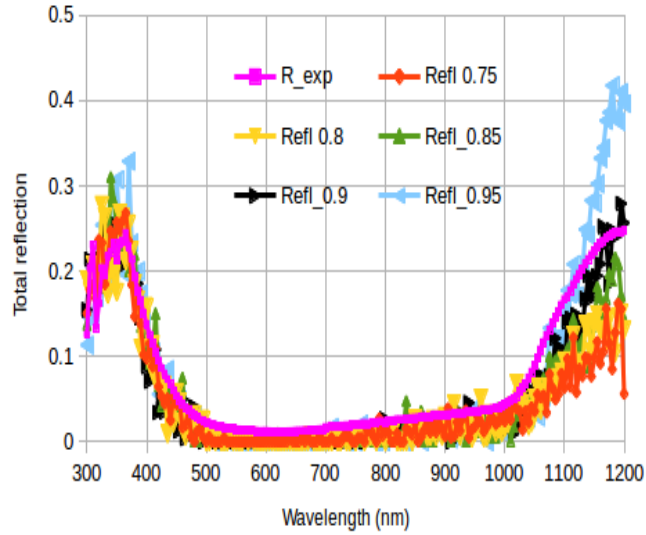


Figure 2.24: Reflection for different values of rear reflectivity

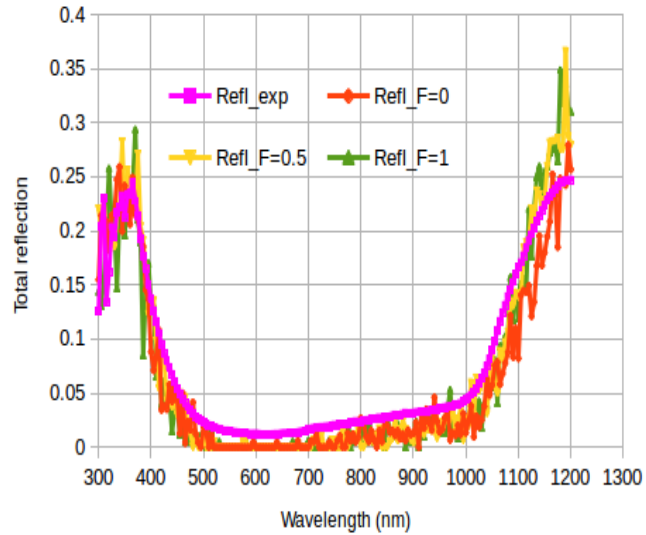


Figure 2.25: Reflection for different values of scattering fraction F

Then we had to select values of front and rear pyramid parameters. Since pyramid height has negligible effect on output parameters, we used  $5 \mu\text{m}$  height for both side pyramids. We plotted reflection for different values of front and rear pyramid angle as follows.

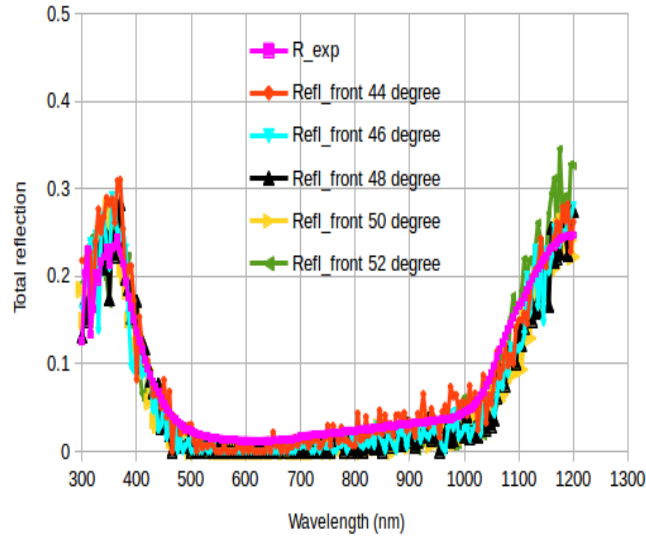


Figure 2.26: Reflection for different values of front pyramid angle

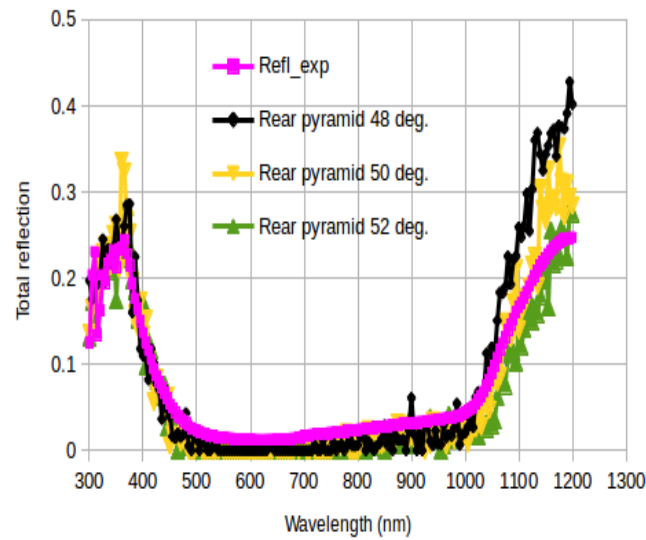


Figure 2.27: Reflection for different values of rear pyramid angle

From above analysis, we reached at a set of parameters which is best suitable for this study. Table 2.9 lists these parameters of wafer ray tracer.

Table 2.9: Input parameters in wafer ray tracer for good fitting

Input parameter	Value
SiN <sub>x</sub> model	PECVD 2.09 (Vog15)
SiN <sub>x</sub> thickness	75 nm
Rear reflectivity	90 %
Lambertian scattering fraction	0
Front pyramid angle	48°
Front pyramid height	5 μm
Rear pyramid angle	51°
Rear pyramid height	5 μm

### 2.2.3 OPAL2 simulation

Input parameters and structure derived for wafer ray tracer (table 2.9) were used in OPAL2 to obtain reflection. We compared simulated reflection from OPAL2 with experimentally measured reflection in fig. 2.28. It shows that OPAL2 is not accurate in long wavelength range.

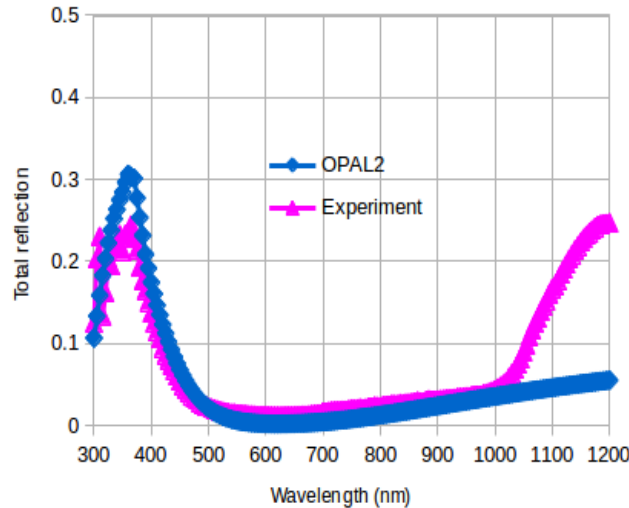


Figure 2.28: Measured cell reflection and simulated reflection from OPAL2

## 2.3 Results and discussion

**Comparison of structure with 100% (ideal case) and 85% (real case) reflectivity in Sunsolve**– All input parameters except rear reflectivity are same as shown in table 2.7. By comparing these two structures, we can calculate parasitic loss. Loss due to poor collection can be obtained by taking the difference of bulk absorptance and IQE currents as mentioned below. ARC reflection, escape reflection and ARC absorption for cell will be same as for structure with 85% rear reflectivity.

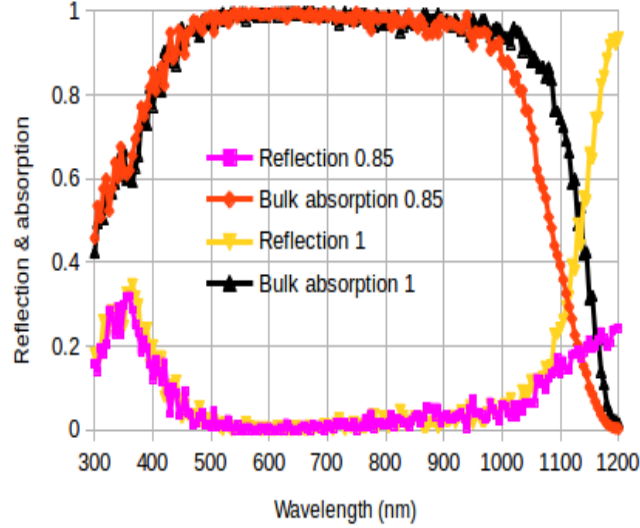


Figure 2.29: Reflection and absorption for rear reflectivity of 85% and 100%

Table 2.10: Output parameters in  $mA/cm^2$  for structure with different rear reflectivity

Rear reflectivity	ARC refl.	Escape refl.	Bulk abs.	ARC abs.	Rear abs.
85%	1.5	0.62	40.61	0.29	3.24
100%	1.51	2.14	42.28	0.36	0

Parasitic loss = difference in reflection+ difference in bulk absorptance+ difference in ARC absorption for both cases

$$= (2.14-0.62) + (42.28-40.61) + (0.36-0.29) = 3.26 \text{ mA/cm}^2$$

Collection loss = bulk absorptance for cell – IQE of cell

$$= 40.61-40.1 = 0.51 \text{ mA/cm}^2$$

Different losses in cell current (or quantum efficiency) can be seen in fig 2.30 along with quantitative description of losses in fig 2.31 and table 2.11.

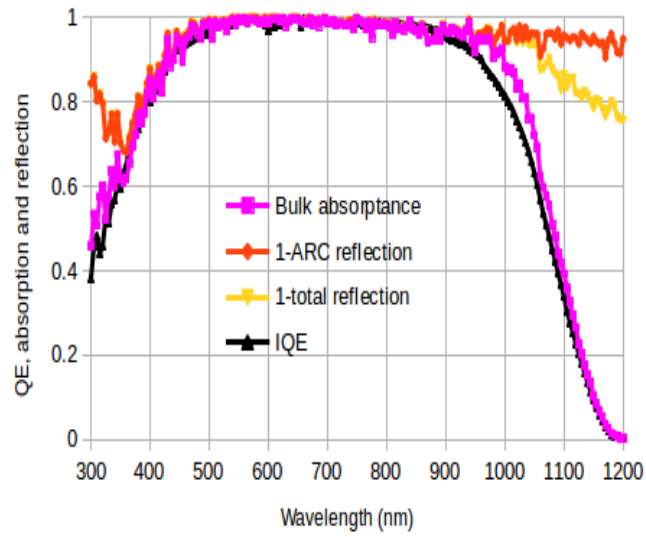


Figure 2.30: QE, bulk absorptance and (1- reflection) for cell

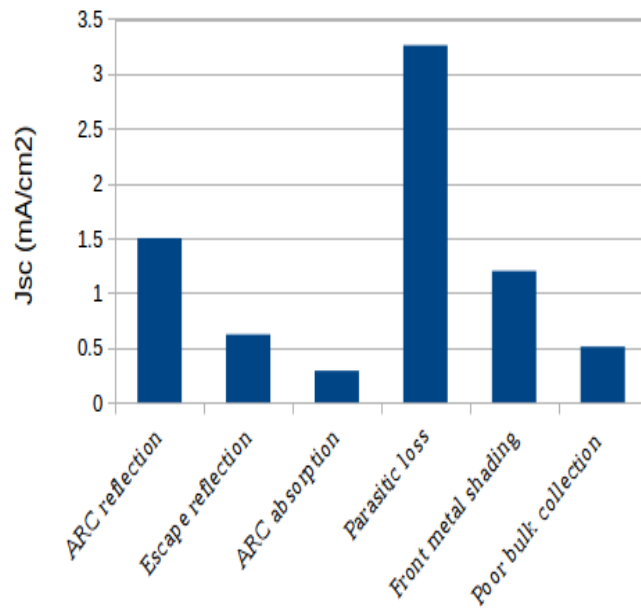


Figure 2.31: Summary of  $J_{sc}$  loss

Table 2.11: Summary of  $J_{sc}$  loss

Type of $J_{sc}$ loss	Value ( $mA/cm^2$ )
Rear parasitic absorption	3.62
ARC reflection	1.5
Front metal shading	1.2
Escape reflection	0.62
Poor bulk collection	0.51
ARC absorption	0.29
Total loss	7.38
$J_{sc}$ from IQE considering shading	38.9

$$J_{sc} \text{ from IQE+ total loss} = 46.3 \text{ mA/cm}^2$$

Loss in  $J_{sc}$  is dominated by parasitic absorption in rear of cell which is  $3.26 \text{ mA/cm}^2$ . In-depth analysis of this loss and underlying parameters is important to reduce this loss. Second large contributor is reflection from  $\text{SiN}_x$  ( $1.62 \text{ mA/cm}^2$ ) which needs to be minimized by optimizing parameters of  $\text{SiN}_x$ . Front metal shading also adds significant amount to the loss and it requires careful and optimized design of fingers and busbars.

### Effect of rear pyramid height on output parameters

As we have observed that parasitic loss is a major contributor of current loss, we need to find some way to reduce this loss. We increased rear pyramid height and analyzed its impact on parasitic loss for  $\text{SiN}_x + \text{Si} + \text{SiN}_x + \text{rear Al}$  structure.

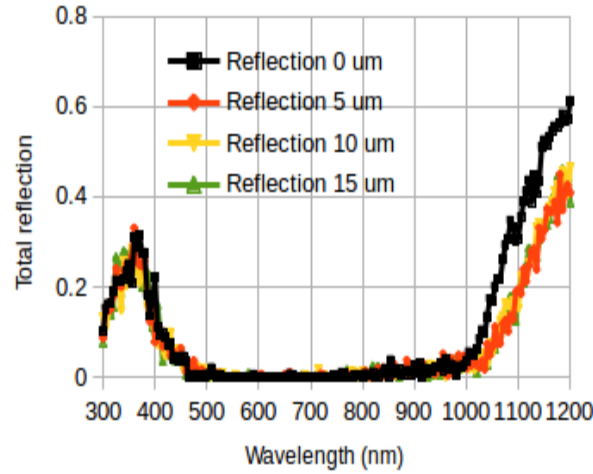


Figure 2.32: Reflection in  $\text{SiN}_x + \text{Si} + \text{SiN}_x + \text{Al}$  for different rear pyramid height

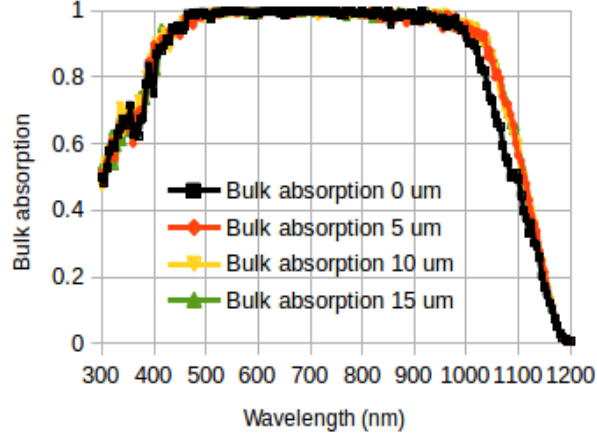


Figure 2.33: Absorption in  $\text{SiN}_x + \text{Si} + \text{SiN}_x + \text{Al}$  for different rear pyramid height

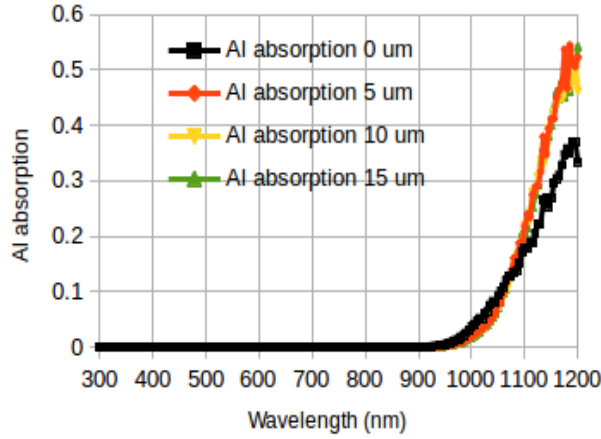


Figure 2.34: Al absorption in  $\text{SiN}_x + \text{Si} + \text{SiN}_x + \text{Al}$  for different rear pyramid height

Table 2.12: Output parameters in  $\text{mA}/\text{cm}^2$  for different rear pyramid height

Height ( $\mu\text{m}$ )	ARC refl.	Escape refl.	Bulk abs.	ARC abs.	Trans.	rear $\text{SiN}_x$ abs.	Al abs.
0	0.9	2.2	41.35	0.32	0	0.09	1.41
5	0.93	1.16	42.04	0.33	0	0.12	1.72
10	0.86	1.25	42.09	0.33	0	0.12	1.65
15	0.87	1.22	42.11	0.33	0	0.12	1.66

**Observation** – Although output parameters are very less sensitive to pyramid height, there is improvement in bulk absorption with increase in rear pyramid height due to reduction in overall reflection and parasitic absorption. It indicates that parasitic losses can be slightly reduced by confining more light at rear with pyramids of a appropriate height.

## 2.4 Comparison of Wafer ray tracer, OPAL2 and Sunsolve

Table 2.13 lists output parameters for sunsolve, wafer ray tracer and OPAL2 along with % difference in output of wafer ray tracer and OPAL2 with respect to sunsolve. Here % difference has been calculated using

% difference = (Difference in value of a parameter in wafer ray tracer or OPAL2 from sunsolve) / (value of that parameter in sunsolve)

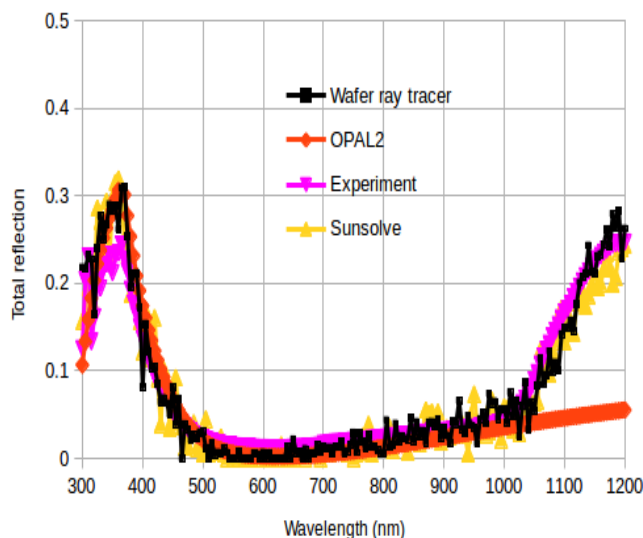


Figure 2.35: Reflection from Wafer ray tracer, OPAL2, Sunsolve and Experiment

Table 2.13: Output parameters in Sunsolve, Wafer ray tracer and OPAL2 (in  $mA/cm^2$ ) and % difference with respect to Sunsolve

$J_{sc}$ loss ( $mA/cm^2$ ) due to	Sunsolve	Wafer ray tracer	% diff.	OPAL2	% diff.
ARC reflection	1.5	1.54	2.6	1.47	2
ARC absorption	0.29	0.24	17	0.26	10.3
Escape reflection	0.62	0.65	4.8	-	-
Parasitic absorption	3.26	3.17	2.7	-	-
Bulk collection loss	0.51	0.86	68	-	-

From above table, we can see that output parameters in wafer ray tracer are in very good agreement with the values in sunsolve. The small difference can vary with structures and input parameters. Therefore, depending on allowable % difference and wavelength range, we can use wafer ray tracer or OPAL2 for current loss analysis in our cell.



# Chapter 3

## Open Circuit Voltage Loss Analysis

Solar cell open circuit voltage is given as-

$$V_{oc} = V_i \ln\left(\frac{J_L}{J_o}\right) \quad (3.1)$$

This equation shows that diode recombination current density  $J_o$  and illumination current density  $I_L$  affect cell open circuit voltage  $V_{oc}$ . Generally, variation in  $I_L$  is very small and hence  $V_{oc}$  is governed by  $J_o$ . Therefore, loss in  $V_{oc}$  can be calculated in terms of recombination current which can take place at different regions in cell. To analyze effect of region specific recombination, we compared structures in intermediate process steps for finding recombination introduced by a particular process or region.

### 3.1 Methodology

To find recombination current in different regions of cell, we have prepared some partially processed structures shown in figure 3.1. Structure A is symmetric lifetime structure with phosphorous diffusion and  $\text{SiN}_x$  coating on both surfaces of Si wafer. Structure B is same as full cell (structure D) except it does not have front metal contact. After etching back Al from this structure, we obtained structure C. Due to unavailability of etching of full 6"x6" sample B, we had to cut this sample before Al etching which gives size of sample C as 2.2"x1.8".

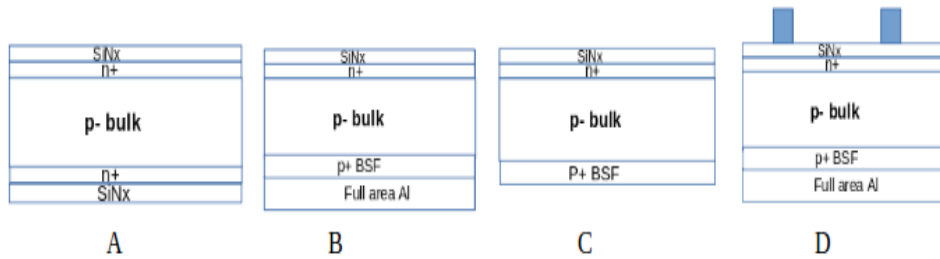


Figure 3.1: Different structures fabricated for  $V_{oc}$  loss analysis

By comparing recombination current of these structures, effect of a particular process step or deposition of layer/film on  $V_{oc}$  of a cell can be estimated. For example, Using difference of recombination in sample A (lifetime structure) and B, quality of bulk and

rear passivation can be examined. similarly by comparing structures B and C, rear metal recombination can be quantified. By comparing structures B and D, loss due to front metal recombination can be estimated. The emitter saturation current density ( $J_{oe}$ ) has been estimated from structure A. For structures B, C and D, two diode model analysis was done and first and second diode saturation current densities, namely  $J_{o1}$  and  $J_{o2}$  were estimated. This analysis helps in extraction of saturation current densities arising from the emitter ( $J_{oe}$ ), combined bulk and rear passivated surface ( $J_{o,base,pass}$ ), rear metal contacts ( $J_{o,rear,met}$ ), junction ( $J_{o2,jun}$ ) and the front metallization ( $J_{o,front,met}$ ). fig. 3.2 shows recombination current in different regions of cell.

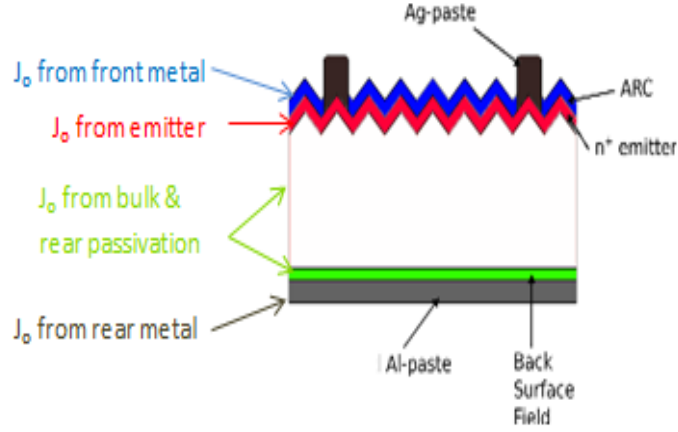


Figure 3.2: Different structures fabricated for  $V_{oc}$  loss analysis

### 3.1.1 Use of Suns- $V_{oc}$ for $V_{oc}$ loss analysis

To determine  $J_{o1}$  and  $J_{o2}$  of structures B, C and Cell, we performed suns- $V_{oc}$  measurement by illuminating the sample at different light intensity or suns. However, this measurement was uncertain as value of  $J_{o2}$  was coming different for sample B and C for three consecutive measurements. This can be probably due to the absence of front metal contacts. For each measurement, the pressure on the probes used for  $Suns - V_{oc}$  measurement may be different as it was done manually.

After facing these issues, we thought of using suns-PL measurement to estimate  $J_{o1}$  and  $J_{o2}$  as this was a non-contact method. Further this method is capable of providing a spatial distribution of recombination parameters over the entire cell area.

### 3.1.2 Use of Suns-PL for $V_{oc}$ loss analysis

PL imaging provides a basis for the measurement of recombination currents in a sample. At certain illumination intensity of LEDs (light source) in PL imaging tool, the luminescence photon flux density  $\phi$  incident on the camera system is related to pn product of cell by following equation [10].

$$\phi = x.(pn - n_i^2) = x.\delta n(\delta n + N_A) \quad (3.2)$$

where  $\phi$  is number of photons per second per unit area per unit solid angle; p and n are the concentrations of free holes and electrons, respectively;  $\delta n$  is the excess carrier

concentration;  $N_A$  is the background doping concentration and  $x$  is a calibration constant which is related to the optical properties of the sample.

To check applicability of Suns-PL method, we plotted PL count and pn product for cell (structure D) on the same curve for different values of suns (or light intensity). These number of suns were derived by measuring current of this cell at 1 sun from I-V measurement and comparing it with current of cell from Greateyes (PL imaging) tool at different light intensities.

pn product of cell was derived from excess carrier concentration obtained from Suns- $V_{oc}$  experiment. Exposure time while taking PL images was 30 sec which was maximum possible time in the tool. PL count was averaged over cell area and corrected by subtracting short circuit PL count from corresponding open circuit PL count to remove background noise. Here open and short circuit PL count correspond to PL images of cell taken at open and short circuit, respectively.

Figure 3.3 shows this curve and clearly indicates linear relation between PL count and pn product of cell. pn product has been scaled to match the range of PL count. By taking average ratio of these two quantities, calibration constant  $x$  can be derived. This calibration constant was calculated to be 70000 for cell and can be used to convert PL count to pn product which in turn can be used to find implied open-circuit voltage by using equation 3.3.

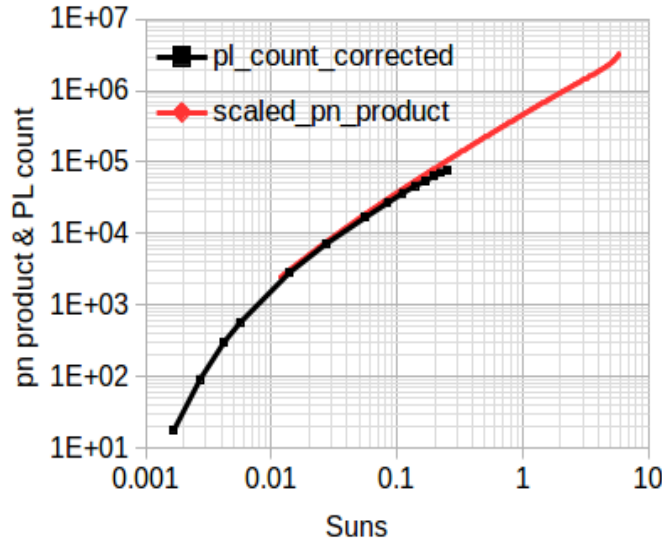


Figure 3.3: pn product and corrected (open-short) PL count for cell

$$iV_{oc} = \frac{kT}{q} \ln\left(\frac{pn}{n_i^2}\right) = \frac{kT}{q} \ln(x * PLcount) \quad (3.3)$$

In the similar manner, we obtained PL count of sample B and C at different light intensities (or suns) and converted it to corresponding pn product to obtain their implied  $V_{oc}$ . Since these samples do not have front contact, we have taken only open circuit PL images (or PL count) for these samples. These PL counts have been shown in fig 3.4.

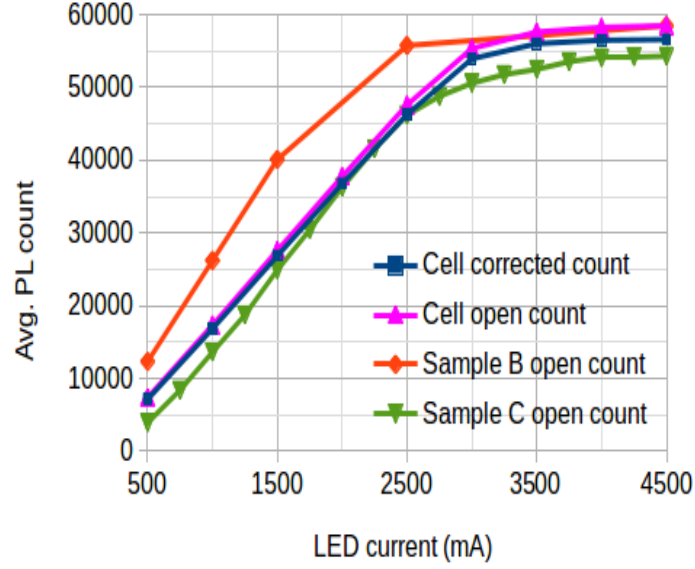


Figure 3.4: Average PL count for cell, sample B and sample C

There are mainly two observations which can be drawn from the curve in fig. 3.3 (a) PL count of all samples is saturating at higher values of LED current which is due to pixel limit of camera used in PL imaging tool and (b) PL count for sample C is smaller than that of sample B which is contradictory to expected results. The second observation drew our attention to the point that since hand cutter was used to cut sample C, this can introduce lots of defects near the edges of this sample. To verify this, we cropped edges of PL images for sample C with the help of MATLAB program. Fig. 3.5 shows that PL count of sample C significantly improves after cropping.

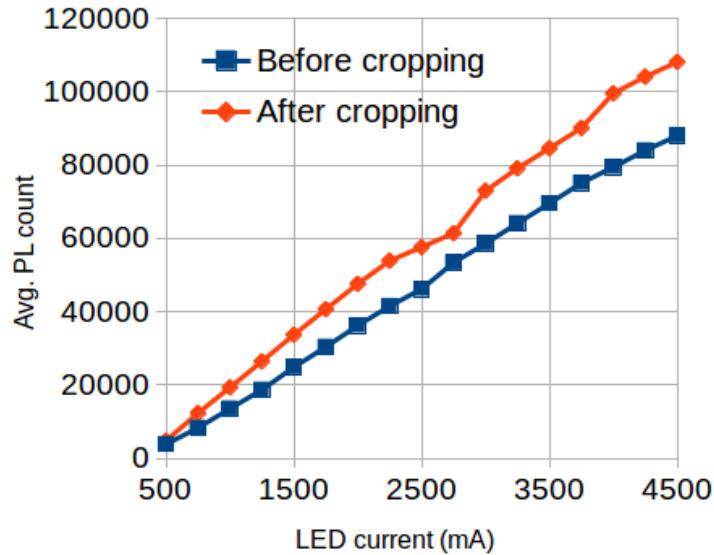


Figure 3.5: Average PL count for sample C before and after edge cropping

To mitigate the effect of saturation at higher LED current, we took PL images for 2

second of exposure time and scaled it with a constant 15 to get equivalent 30 second PL image. After applying these two corrections, we plotted PL count for all 3 samples in fig. 3.6.

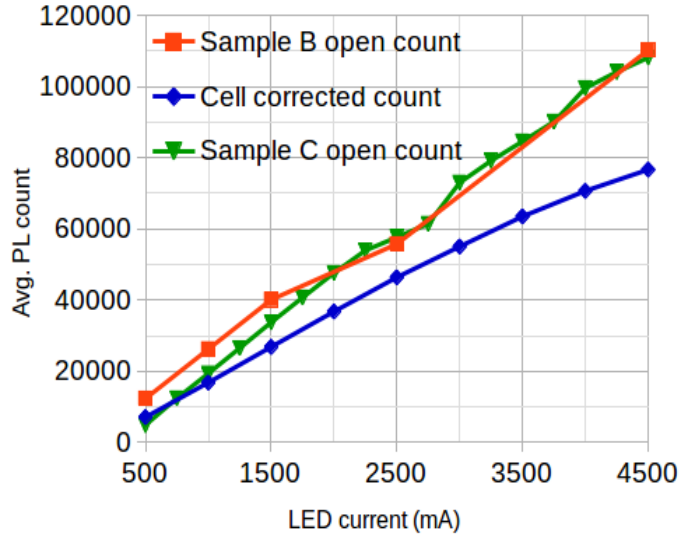


Figure 3.6: Average PL count for cell, sample B and sample C after correction

It is clearly visible that now PL count of sample C is higher than cell and comparable to sample B. These corrected PL counts can be converted to implied  $V_{oc}$  by using calibration constant of respective samples.

To find calibration constant of samples B and C, we used following equation [1] to see dependence of this constant on various parameters.

$$x = \int \frac{1}{4\pi n(\lambda)^2} \frac{A_{BB}(\lambda)}{\alpha_{BB}(\lambda)} B(\lambda) d\lambda \quad (3.4)$$

where  $n(\lambda)$  is the refractive index of silicon;  $A_{BB}$  is the band-to-band absorptance of the sample and  $\alpha_{BB}$  is the band-to-band absorption coefficient; and  $B$  is the volumetric spectral radiative recombination coefficient, which is constant [11]. Equation 3.4 shows that  $x$  depends on bulk absorptance and hence reflection from rear surface. To verify this argument, we plotted reflection of all three samples on same curve in fig. 3.7 which shows that near the emission band (1100 nm), there is significant difference in reflection of these samples which is due to their different rear structure and hence rear reflection.

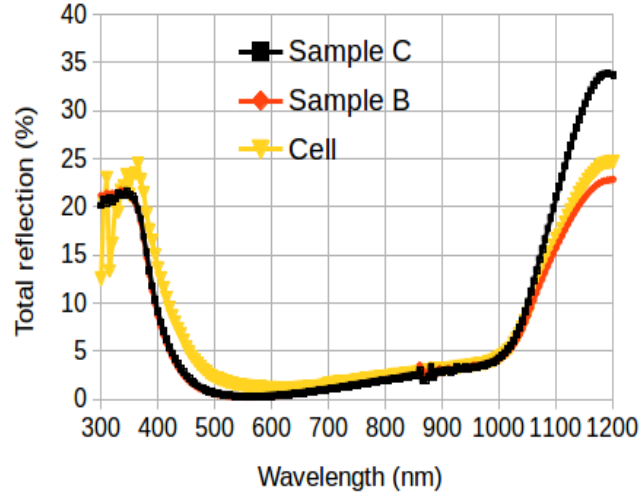


Figure 3.7: Measured reflection for cell, sample B and sample C

Sample C has highest rear reflection due to absence of rear Al which absorbs significant light. Ideally sample B and cell should have same rear reflectance due to similar rear structure, but they slightly differ. We suspect that its reason can be variation in firing conditions of front metal in these two samples.

By taking ratio of reflection of samples B and C to the cell reflection at 1100 nm, we calculated calibration constant for these samples; it was 68557 and 93814 for B and C, respectively. First we plotted PL count for all samples.

Since incident light or number of suns are same for all samples, current density  $J_{sc}$  will also remain same. We plotted  $J_{sc} - iV_{oc}$  curve for all samples in following figure.

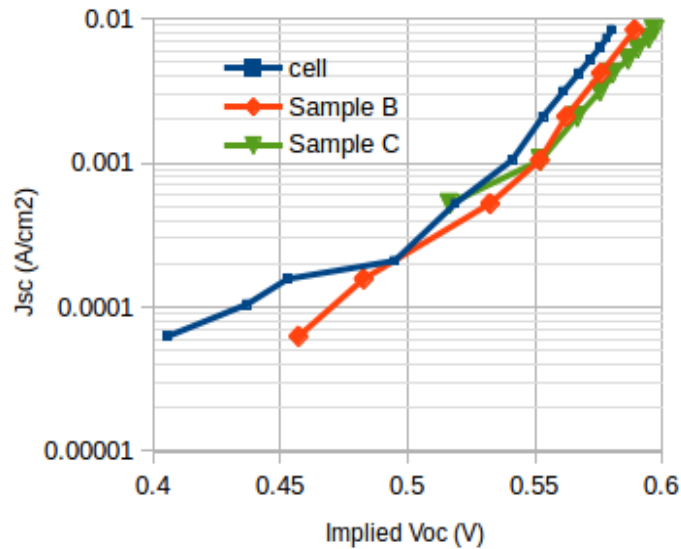


Figure 3.8:  $J_{sc} - iV_{oc}$  curve for cell, sample B and sample C

These  $J_{sc} - V_{oc}$  curves can be analyzed using double diode model for solar cells.

$$J_L = J_{o1}[\exp(\frac{q(V + JR_s)}{kT}) - 1] + J_{o2}[\exp(\frac{q(V + JR_s)}{2kT}) - 1] + \frac{V + JR_s}{R_{sh}} \quad (3.5)$$

where  $J_L$  is the light-induced current density, and  $J_{o1}$  and  $J_{o2}$  are the first and second diode recombination current densities, respectively.

## 3.2 Results and discussion

Table 3.1: Summary of  $V_{oc}$  losses due to different regions in cell

Sample/ region	$J_{o1}(10^{-13})A/cm^2$	$J_{o2}(10^{-9})A/cm^2$
D (cell)	11.2	9.6
B	7	6.46
C	5.61	2.76
Front metal	$3 (J_{o1(D)} - J_{o1(B)})$	$3.14 (J_{o2(D)} - J_{o2(B)})$
Rear metal	$1.4 (J_{o1(B)} - J_{o1(C)})$	$3.7 (J_{o1(B)} - J_{o1(C)})$
Base, passivation	$4.45 (J_{o1(C)} - J_{oe})$	-
Junction	-	$2.76 (J_{o2(C)})$

Table 3.1 mentions summary of  $V_{oc}$  loss in cell.  $J_{oe}$  has been calculated using Kane-Swanson method and  $J_{o1}$ ,  $J_{o2}$  measurement have been done by fitting  $J_{sc} - iV_{oc}$  curve using equation 3.5.

Impact of the  $J_{o1}$  and  $J_{o2}$  sources on the cell  $V_{oc}$  can be assessed by the recombination current densities  $J_R$  they generate. These recombination currents are given as  $J_{R1} = J_{o1}\exp(V_{oc}/V_t)$  and  $J_{R2} = J_{o2}\exp(V_{oc}/2V_t)$  for first and second diode, respectively. Total recombination current is sum of recombination currents in these two regions. We converted this recombination currents to equivalent first diode recombination current by dividing total  $J_R$  by  $\exp(V_{oc}/V_t)$ . We obtained following distribution of these recombination mechanisms in cell.

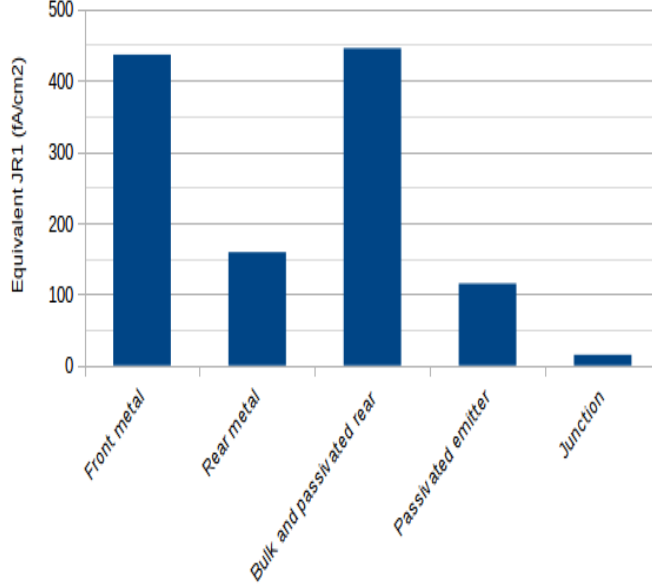


Figure 3.9: Summary of  $V_{oc}$  loss

Table 3.2: Summary of  $V_{oc}$  loss

Equivalent $J_{01}$	Value ( $fA/cm^2$ )
Base and pasivated rear	445
Front metal	437
Rear metal	159
Passivated emitter $J_{oe}$	115
Junction	15

We can see that major loss in cell  $V_{oc}$  is caused by recombination in base and passivated rear. We also calculated rear surface recombination velocity (BSRV) for cell which was around 1221 cm/sec. Very large value of BSRV also correlates high rear recombination and impinges a requirement on improving rear passivation to get benefit in terms of  $V_{oc}$ .

Front grid related recombination is also very large which needs a detailed investigation to find an effective way to reduce this loss.

A slightly lower but yet considerable loss in  $V_{oc}$  is contributed by recombination in rear metal. After reducing front metal and base & passivated rear losses, if we want to achieve a gain in  $V_{oc}$  then rear contact parameter optimization should be next logical step. Emitter passivation is better as shown by low value of emitter saturation current ( $115 fA/cm^2$ ). Junction recombination is least among all ( $15 fA/cm^2$ ) and verifies good quality of junction in our cell.



# Chapter 4

## Fill Factor Loss Analysis

Short circuit current and open circuit voltage collectively describe maximum possible power out of cell. However, actual power generation capability of cell is governed by its fill factor. Fill factor is affected by  $J_{o1}$ ,  $J_{o2}$  and series and shunt resistance ( $R_s$  and  $R_{sh}$  of cell. To examine the relationship of fill factor with these parameters, we have plotted FF with  $J_{o2}$  in figure 4.1 and with  $R_{sh}$  in figure 4.2 for a generalized case. These figure clearly describe that FF strongly depends on these parameters.

We have calculated  $J_{o1}$  and  $J_{o2}$  for our cell from I-V curve based on two diode model. Series resistance  $R_s$  has been calculated by considering pseudo I-V curve (from  $Suns-V_{oc}$ ) and actual IV curve at maximum power point [7]. Shunt resistance  $R_{sh}$  has been extracted from slope of dark I-V curve in voltage range -50 mV to +50 mV. These values have been mentioned in table 4.1.

We have calculated FF loss due to various components using method given by Khanna *et. al* [12] discussed in details in subsequent sections. This method requires  $R_s$ ,  $R_{sh}$ ,  $V_{oc}$ ,  $J_{sc}$ ,  $V_{mpp}$  and  $J_{mpp}$ .

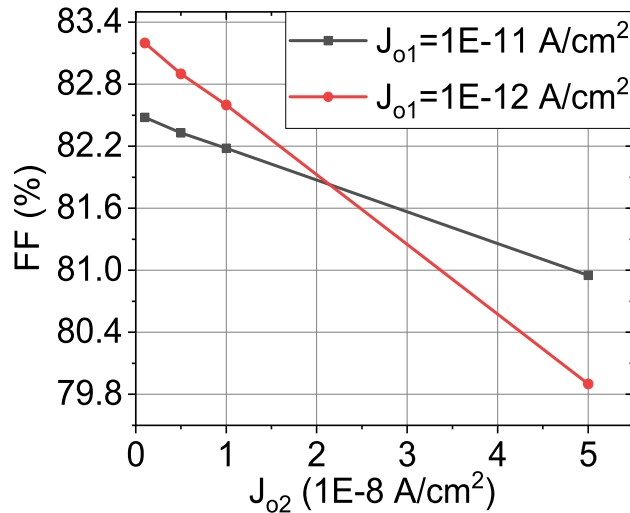


Figure 4.1: Fill factor variation with  $J_{o2}$

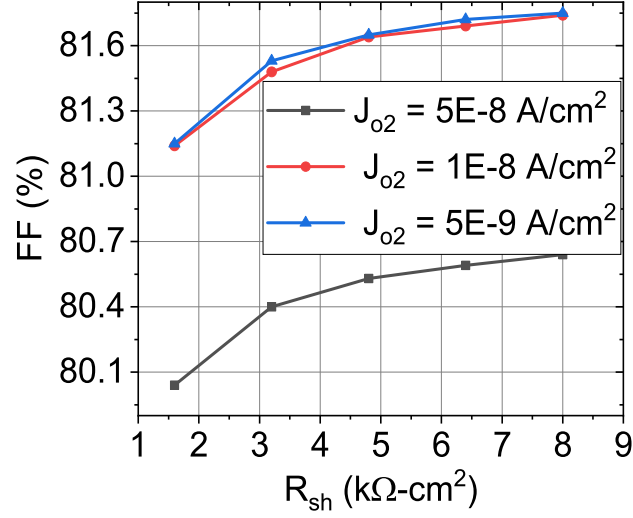


Figure 4.2: Fill factor variation with  $R_{sh}$

Table 4.1: Recombination current and resistive components for cell

Parameter	Value
$J_{o1}$ (A/cm²)	8.27E-13
$J_{o2}$ (A/cm²)	1.82E-8
$R_s$ (mΩ - cm²)	280
$R_{sh}$ (kΩ - cm²)	8.1

## 4.1 Methodology

Equation 4.1 describes I-V characteristics of diode assuming two diode model.

$$J = J_{ph} - J_{o1} \left( \exp\left(\frac{V + JR_s}{V_t}\right) - 1 \right) - J_{o2} \left( \exp\left(\frac{V + JR_s}{2V_t}\right) - 1 \right) - \frac{(V + JR_s)}{R_{sh}} \quad (4.1)$$

### 4.1.1 $J_{o1}$ limit of FF

If we assume that  $J_{o2}$ ,  $R_s$  and  $R_{sh}$  are absent, then FF is limited by recombination in bulk and surfaces. In this case equation 4.1 reduces to

$$J = J_{sc} - J_{sc} \frac{\exp\left(\frac{V}{V_t}\right) - 1}{\exp\left(\frac{V_{oc}}{V_t}\right) - 1} \quad (4.2)$$

Fill factor of J-V curve in equation 4.2 is  $J_{o1}$  limited FF.

### 4.1.2 FF loss due to $R_s$ and $R_{sh}$

In two diode model, terminal voltage and current ( $V_o$  and  $J_o$ ) are related to  $V_{mpp}$  and  $J_{mpp}$  as follows -

$$V_{mpp} = V_o - J_{mpp}R_s \quad (4.3)$$

$$J_{mpp} = J_o - \frac{(V_{mpp} + J_{mpp}R_s)}{R_{sh}} \quad (4.4)$$

When these equations are solved, we get FF loss due to  $R_s$  and  $R_{sh}$  given in equation 4.5 and 4.6, respectively.

$$\Delta FF_{R_s} = \frac{(J_{mpp})^2 R_s}{V_{oc} J_{sc}} \quad (4.5)$$

$$\Delta FF_{R_{sh}} = \frac{(V_{mpp} + J_{mpp}R_s)^2}{R_{sh} V_{oc} J_{sc}} \quad (4.6)$$

### 4.1.3 FF loss due to $J_{o2}$

FF loss due to  $J_{o2}$  is given by finding the difference between the  $J_{o1}$  limit of fill factor and the resistance free fill factor.

$$\Delta FF_{J_{o2}} = FF_{J_{o1}} - FF_o \quad (4.7)$$

Here  $FF_o$  is resistance free fill factor.

## 4.2 Results and discussion

Upper limit on FF imposed by  $J_{o1}$  is 83.18 % for cell under study. Remaining loss factors have been shown in bar chart of figure 4.3 and table 4.2. Series resistance is dominating loss in FF followed by second diode saturation current  $J_{o2}$ . Impact of both of these parameters pulls FF to a low value.  $R_s$  is a lumped parameter which combines series resistance of front and rear metal, emitter, bulk, rear and both surfaces. To quantify series resistance loss in more detail, we can find contribution of individual component in FF loss of cell and put our efforts to optimize appropriate process or device parameters.

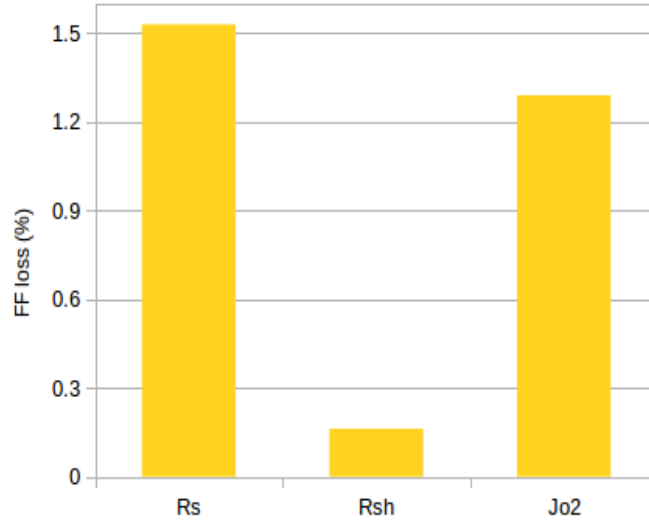


Figure 4.3: Summary of fill factor loss

Table 4.2: Summary of fill factor loss for cell

Loss	Value (%)
$J_{o1}$ limited FF	83.18
$\Delta FF_{Rs}$	1.53
$\Delta FF_{Rsh}$	0.162
$\Delta FF_{Jo2}$	1.29
Total loss	2.982
Measured FF	80.2
Error	0.002

## Chapter 5

# Calculation and Mapping of Diffusion Length and Back Surface Recombination Velocity

Current of solar cell has contribution from different regions e.g., emitter, depletion and base region. If current in each of these regions is not degraded very much then spectral response of cell will be desirable. However, the current is affected either due to poor quality of bulk material or due to poor passivation at front or back surfaces and it is not same as we expect.

Light is shined on front surface of cell to generate electron-hole pairs. Most of the generation happens near this surface. Therefore, quality of this surface should be very good otherwise it will cause undesired conditions e.g., low absorption, reflection of light, recombination of photo-generated carriers at the surface etc which will degrade the response. As soon as electron-hole pairs are generated in the cell, these carriers should be separated to extract current. For this to happen, the lifetime or diffusion length of minority carriers in bulk material should be high enough to allow their collection before they get recombined.. If diffusion length is small, carriers will recombine before reaching junction. Similarly, when light reaches back surface of cell, it might get reflected from this surface or recombination can happen here .

Due to above mentioned problems, response of cell will degrade which will cause reduction in efficiency. To characterize quality of bulk and surface, we use diffusion length (L) and surface recombination velocity (SRV) as respective indicative parameters. Surface recombination velocity tells about rate of recombination of minority carriers at surface of cell. Usually it is little bit complicated to find S and L from spectral response but with the help of some assumptions, calculation of these values becomes simple. In the method used in this work, we have shined light of different wavelengths to penetrate different regions inside the cell and to find current in these regions. The relation between output current and input light comes linear which is known as spectral response and contains information of these parameters.

## 5.1 Methodology

### 5.1.1 Computation of diffusion length

According to the method described by Jain *et al.*[13], L can be computed using the following relation

$$L = \frac{d}{\cosh^{-1} \frac{\zeta_m}{\zeta}} \quad (5.1)$$

Where, d is the thickness of the cell,  $\zeta_m$  is maximum possible spectral response,  $\zeta$  is measured spectral response and can be expressed as

$$\zeta_m = (1 - R) \frac{q\lambda}{hc} \quad (5.2)$$

$$\zeta = IQE \frac{q\lambda}{hc} \quad (5.3)$$

Where R and IQE are reflectance and internal quantum efficiency respectively at the desired wavelength.

Equation (1) illustrates that L will have deterministic value for the condition  $\frac{\zeta_m}{\zeta} > 1$ . Further, this condition can be written as  $\frac{1-R}{IQE} > 1$ . Here, term (1-R) represents the absorbed incident radiation in the cell which will always be greater than the IQE of the cell.

### 5.1.2 Computation of surface recombination velocity

Sharma *et al.* [13] estimated rear surface recombination velocity by measuring IQE and R at two suitable wavelengths  $\lambda_1$  and  $\lambda_2$  as follows

$$SRV = \frac{D_n(L_{\lambda_2} - L_{\lambda_1})}{L_{\lambda_2}L_{\lambda_1}(G - 1)} \quad (5.4)$$

where

$$G = \frac{\zeta_1 \zeta_{m2} L_{\lambda_2}}{\zeta_2 \zeta_{m1} L_{\lambda_1}} \quad (5.5)$$

$D_n$  is the diffusion coefficient of electrons and  $L_{\lambda_1}$  and  $L_{\lambda_2}$  are absorption depth (inverse of the absorption coefficient) for  $\lambda_1$  and  $\lambda_2$ , respectively. Here  $\zeta_1$ ,  $\zeta_{m1}$  and  $\zeta_2$ ,  $\zeta_{m2}$  are measured SR and maximum possible SR for  $\lambda_1$  and  $\lambda_2$ , respectively. It is required that wavelengths  $\lambda_1$  and  $\lambda_2$  should be absorbed in bulk region and near to rear surface (thus includes the effect of surface recombination), respectively, and implies that selected wavelengths fulfil the required condition  $\lambda_2 > \lambda_1$ , i.e.  $L_{\lambda_2} > L_{\lambda_1}$ .

## 5.2 Experimental details

Two different solar cell technologies Al-BSF and PERC carrying different passivation schemes at the back surface have been considered and depicted in figure 5.1. PERC structure incorporates the dielectric passivation layer at the back surface which avoids direct contact between semiconductor and metal, and thus minimizes the recombination of minority carriers at this surface. Capping layer has been used to isolate the dielectric

layer and metal [14]. Four cells of conventional size 6" x 6", namely mono-crystalline Al-BSF (M1), mono-crystalline PERC (M2), multi-crystalline Al-BSF (N1) and multi-crystalline PERC (N2) have been used in this study.

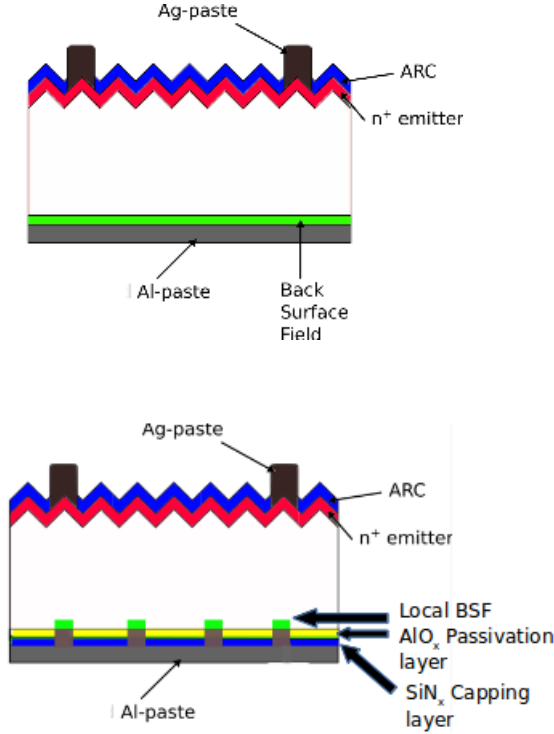


Figure 5.1: Al-BSF and PERC structures of solar cell

Light beam induced current (LBIC) tool was used to generate the spatially distributed data of IQE and R in steps of 500  $\mu\text{m}$  corresponding to excitation wavelengths 877 nm and 984 nm on the full area of solar cell. These two wavelengths fulfil the required condition ( $\lambda_2 > \lambda_1$  and  $L_{\lambda_2} > L_{\lambda_1}$ ) as absorbed in bulk ( $L_\lambda = 20 \mu\text{m}$  for  $\lambda = 877 \text{ nm}$ ) and close to rear surface ( $L_\lambda = 125 \mu\text{m}$  for  $\lambda = 984 \text{ nm}$ ), respectively.

### 5.3 Results and discussion

Computation of L and SRV for all four cells was done using equation 5.4 and 5.5, respectively. The thickness of cell d and diffusion coefficient  $D_n$  of the electrons were taken as 180  $\mu\text{m}$  and 25  $\text{cm}^2/\text{sec}$ , respectively. The constants  $q = 1.602 \times 10^{-19} \text{ C}$ ,  $h = 6.626 \times 10^{-34} \text{ J-s}$  and  $c = 3.0 \times 10^{10} \text{ cm/s}$  with IQE and R values at desired wavelengths were used to compute  $\zeta$  and  $\zeta_m$ .

Fig. 5.2 (a) and 5.2 (b) show distribution of L for cells M1 and N1, respectively. Cell M1 has values of L confined to a small range of 450 - 600  $\mu\text{m}$  while N1 shows a wide distribution range of 150-600  $\mu\text{m}$ , as shown in Fig. 5.2 (c). Such distribution is due to the multi crystalline nature of N1 where grains of different orientation cause the fluctuation in L values [15]. Whereas, M1 being a mono-crystalline cell has no grain boundaries and hence does not suffer from grain boundary recombination. However, magnitude of L in bulk of multi-crystalline cells does not always have similar type of dispersion due to

random distribution of grains and other defects.

These maps are helpful to analyze the effect of annealing at low temperature (500 °C) on bulk quality of cell. This annealing followed by emitter diffusion improves IQE and hence L of multi-crystalline cells especially for wafers cut from borders of the ingots [16]. Similar analysis can be performed to observe the effect of oxidation and  $\text{POCl}_3$  diffusion which improves the bulk quality of mono-crystalline cells [17].

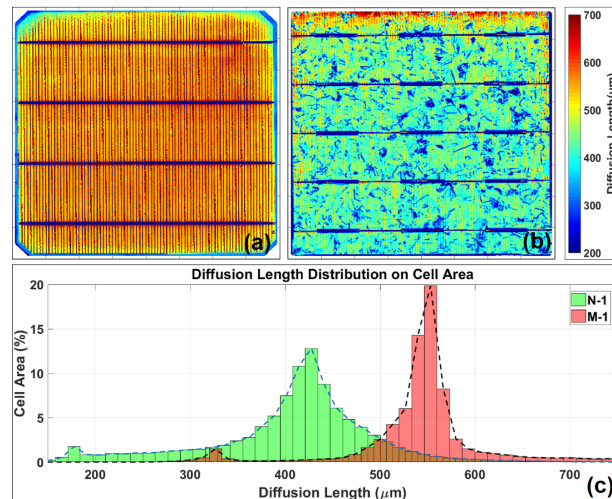


Figure 5.2: Comparison of L values in (a) mono-crystalline (M1) and (b) multi-crystalline cells (N1), Al-BSF cells. (c) shows the histograms of the L over the wafer area.

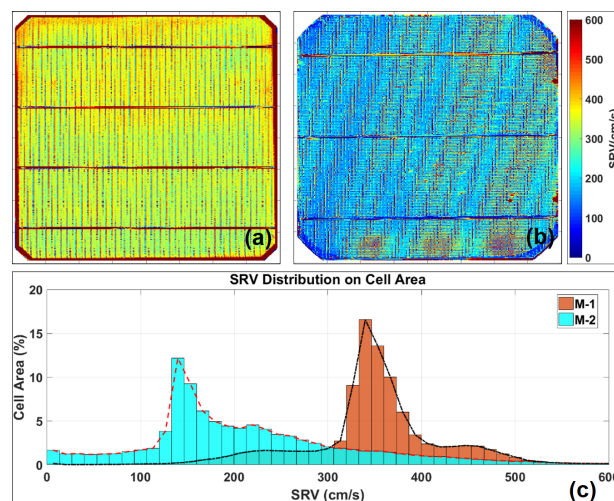


Figure 5.3: Comparison of rear side SRV values in (a) mono Al-BSF (M1) and (b) mono PERC (M2). (c) shows the histograms of the SRV over the wafer area.



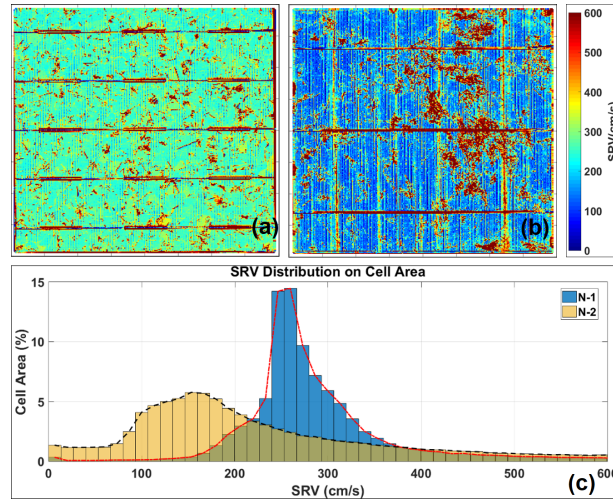


Figure 5.4: Comparison of SRV values in (a) multi Al-BSF (N1) and (b) multi PERC (N2). (c) shows the histograms of the SRV over the wafer area.

Fig. 5.3(a) and (b) show SRV maps for cells M1 and M2, respectively. SRV values for cell M2 were found in the range of 20 - 270 cm/sec lower than 300 - 500 cm/sec for cell M1 as shown in Fig. 5.3(c). This difference shows that the dielectric passivation at the rear surface in PERC cell shows better control on carrier recombination than Al assisted surface passivation in case of Al-BSF cell, also described by S. Gatz *et al.* [18]. Similar investigation was performed for multi-crystalline cells, N1 and N2 and the results are shown in figure 5.4. Higher SRV values (250 - 330 cm/sec) were obtained for cell N1 as compared to N2 (10 - 230 cm/sec), following mono-crystalline cells M1 and M2. Therefore, optimization of surface passivation at rear side of solar cell can be easily done using the methodology presented here. Further, spatial distribution of SRV on cell area will be helpful to achieve better process uniformity.

# Chapter 6

## MATLAB program for loss analysis

After calculating losses in all cell parameters ( $J_{sc}$ ,  $V_{oc}$  and FF), we developed a graphical user interface (GUI) using MATLAB. We created this tool for  $V_{oc}$  and FF loss analysis. Since most of the part of  $J_{sc}$  loss is calculated in sunsolve (or wafer ray tracer), we found no need to make separate tool for  $J_{sc}$  loss analysis.

### 6.1 Details of $V_{oc}$ loss analysis tool

Fig. 7.1 shows screenshot of MATLAB GUI for  $V_{oc}$  loss.

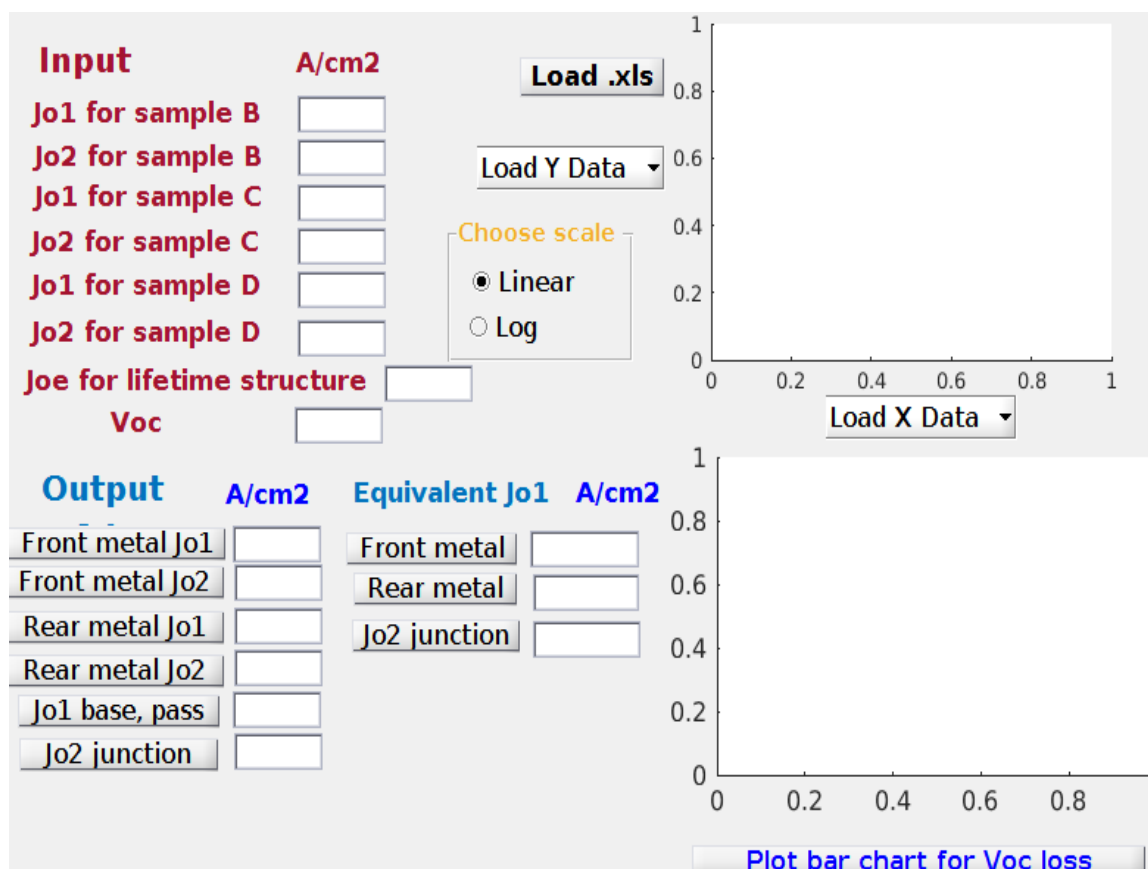


Figure 6.1: GUI for  $V_{oc}$  loss

## Inputs-

### Steps to calculate $J_{o1}$ and $J_{o2}$ for samples -

1. Measure  $J_{oe}$  for sample A.
2. Do PL imaging of sample B at open circuit for range of LED current 500-4500 mA in Greateyes tool and take average PL count at each LED current.
3. Repeat step 2 for sample C.
4. Do PL imaging of sample D at open and short circuit for range of LED current 500-4500 mA and take average PL count at each LED current. Calculate corrected PL count by subtracting short circuit count from corresponding open circuit count.
5. Do Suns- $V_{oc}$  measurement for sample D and calculate pn product for different intensities.
6. Find calibration constant for sample D using its pn product and PL count at common light intensities.
7. Measure reflection for sample B,C and D.
8. Compare reflection of sample B and C with that of cell at 1100 nm. Ratio of reflection is same as ratio of calibration constants. It gives calibration constant for sample B and C. while calculating calibration constant, consider front metal shading which is absent in sample B and C.
9. Convert PL counts of all samples to pn product and hence implied  $V_{oc}$  using their corresponding calibration constants.
10. Find  $J_{sc}$  using light intensity. Due to same illumination,  $J_{sc}$  will be same for all samples.
11. Plot  $J_{sc}$ - $iV_{oc}$  curve for all samples and extract  $J_{o1}$  and  $J_{o2}$  from these curves using two diode model.

After calculating  $J_{o1}$  and  $J_{o2}$  for each sample, we can insert these values and measured  $V_{oc}$  in GUI to find losses due to different components of cell. Apart from this, we can load any data for plotting and see in either linear or logarithmic scale as shown in top right area and check correspondence between results and graph.

**Outputs-** As we can see, this tool provides loss due to individual component in cell-front metal, rear metal, junction, base & passivated rear and passivated emitter. Furthermore, for each component, it calculates contribution to first and second diode saturation current density  $J_{o1}$  and  $J_{o2}$ . All these losses can be converted to equivalent first diode saturation current density  $J_{o1}$  and can be plotted in the form of bar chart on bottom right area.

## 6.2 Details of FF loss analysis tool

Fig. 7.2 shows screenshot of MATLAB GUI for FF loss.

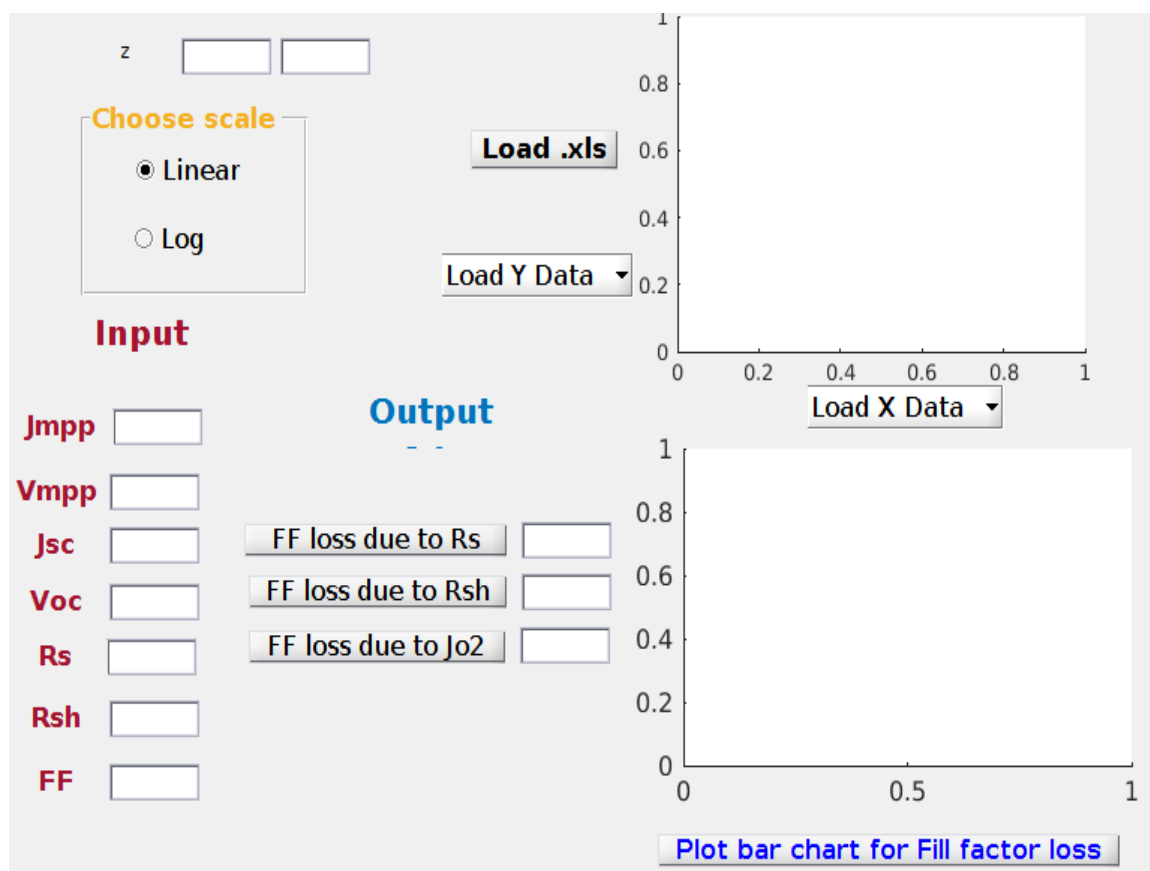


Figure 6.2: GUI for FF loss

**Inputs-** Here, we need to have light and dark I-V parameters -  $J_{mpp}$ ,  $V_{mpp}$ ,  $J_{sc}$ ,  $V_{oc}$ , measured FF,  $R_s$  and  $R_{sh}$ . Again, it is possible to load any data for plotting on appropriate scale.

**Outputs-** Loss in FF due to  $R_s$ ,  $R_{sh}$  and  $J_{o2}$  is displayed at the output and plotted in the form of bar chart.

## 6.3 Details of $J_{sc}$ loss analysis

ARC reflection, escape reflection and ARC absorption can be directly obtained from sunsolve or wafer ray tracer simulation. Front metal shading calculation needs  $J_{sc}$  from IV and EQE measurements. Procedure of rear parasitic and bulk collection loss estimation also has been described in section 2.2.

**Link of MATLAB codes for Voc and FF loss analysis - [Click here](#)**

# Chapter 7

## Conclusion and Future Work

### 7.1 Conclusion

Performance of solar cell is governed by its electrical parameters which are  $J_{sc}$ ,  $V_{oc}$  and FF. Therefore, it is extremely important to analyze losses in these parameters and take necessary actions to minimize them. We have calculated loss in these parameters in detail. Loss in  $J_{sc}$  is dominated by parasitic absorption and ARC reflection both of which should be controlled by optimizing appropriate parameters. Although sunsolve gives most accurate simulation results for current loss analysis, It is also possible to get a considerably good fitting in wafer ray tracer by iterating its input parameters one by one. However, OPAL2 is not a good choice when analysing losses in rear regions of cell (or long wavelengths). However, parameters of ARC can be optimized using OPAL2 since its accuracy is good for short wavelength. We obtained process parameters and thickness of  $SiN_x$  for minimum reflection and absorption in this layer. Optimization of front metal grid and rear passivation is crucial to obtain large value of  $V_{oc}$ . Loss in FF due to shunt resistance is negligible since shunt is very large.  $R_s$  loss is dominant in FF loss of cell.

We also calculated diffusion length in bulk and surface recombination velocity at rear side of solar cells using quantum efficiency and reflectance. It was observed that multi-crystalline cells exhibit wider distribution of diffusion length in comparison to mono-crystalline cells because of grains boundaries present in the bulk of multi crystalline wafers. PERC cells (mono and multi-crystalline) show smaller values of surface recombination velocity attributed to superior passivation at rear side in comparison to the Al-BSF cells. This analysis helps in assessment of bulk quality and rear surface passivation which is critical for the development of large area solar cells with high efficiency.

### 7.2 Future work

Similar loss analysis can be extended to different quality wafer cells and different structures of cell e.g., multi-crystalline and PERC cell. Rear parasitic loss in cell can be further broken down to loss due to individual layer in rear such as Al-BSF, Si-Al alloy and Al. We have neglected loss in emitter region in this study but this needs to be analyzed and estimated accurately for more accurate analysis.

# References

- [1] J. Wong, S. Duttagupta, R. Stangl, B. Hoex, and A. G. Aberle, “A systematic loss analysis method for rear-passivated silicon solar cells,” *IEEE Journal of Photovoltaics*, vol. 5, pp. 619–626, March 2015.
- [2] N. Gupta, G. Alapatt, R. Podila, R. Singh, and K. Poole, “Prospects of nanostructure-based solar cells for manufacturing future generations of photovoltaic modules,” *International Journal of Photoenergy*, vol. 2009, 10 2009.
- [3] Electrical4U, “Characteristics of a solar cell and parameters of a solar cell.” <https://www.electrical4u.com/about/>, Apr. 2019.
- [4] R. A. Tegio, “The difference between standard and perc solar cells.” <https://www.azom.com/article.aspx?ArticleID=16715>, May 2019.
- [5] P. Ščajev, *Investigation of wide-band-gap semiconductor photoelectric properties by using optical techniques with temporal and spatial resolution*. PhD thesis, 01 2013.
- [6] D. E. Kane and R. M. Swanson, “Measurement of the emitter saturation current by a contactless photoconductivity decay method,” 1985.
- [7] A. G. Aberle, S. R. Wenham, and M. A. Green, “A new method for accurate measurements of the lumped series resistance of solar cells,” in *Conference Record of the Twenty Third IEEE Photovoltaic Specialists Conference - 1993 (Cat. No.93CH3283-9)*, pp. 133–139, May 1993.
- [8] PVLighthouse. <https://www.pvlighthouse.com.au/>, 2011.
- [9] T. H. Fung, M. U. Khan, Y. Zhang, N. J. Western, D. N. R. Payne, K. R. McIntosh, and M. D. Abbott, “Improved ray tracing on random pyramid texture via application of phong scattering,” *IEEE Journal of Photovoltaics*, vol. 9, no. 3, pp. 591–600, 2019.
- [10] T. Trupke, R. A. Bardos, and M. D. Abbott, “Self-consistent calibration of photoluminescence and photoconductance lifetime measurements,” *Applied Physics Letters*, vol. 87, no. 18, p. 184102, 2005.
- [11] P. P. Altermatt, F. Geelhaar, T. Trupke, X. Dai, A. Neisser, and E. Daub, “Injection dependence of spontaneous radiative recombination in crystalline silicon: Experimental verification and theoretical analysis,” *Appl. Phys. Lett.*, vol. 88, pp. 261901–1–261901–3, 2006.
- [12] A. Khanna, T. Mueller, R. A. Stangl, B. Hoex, P. K. Basu, and A. G. Aberle, “A fill factor loss analysis method for silicon wafer solar cells,” *IEEE Journal of Photovoltaics*, vol. 3, pp. 1170–1177, Oct 2013.

- [13] A. K. Sharma, S. Singh, N. Bisht, H. Khandpal, and Z. Khan, “Effect of air ambient on surface recombination and determination of diffusion length in silicon wafer using photocurrent generation method,” *Solar Energy*, vol. 85, pp. 1137–1143, 05 2011.
- [14] E. Urrejola, J. Hong, C. Charpentier, A. Zauner, S. Pouliquen, and A. Madec, “Dielectric capping layers for high efficiency rear passivated silicon solar cells,” 09 2014.
- [15] S. Zhou, Z. Chunlan, W. Wang, Y. Tang, J. Chen, B. Yan, and Y. Zhao, “Effect of subgrains on the performance of mono-like crystalline silicon solar cells,” *International Journal of Photoenergy*, vol. 2013, 10 2013.
- [16] M. Rinio, A. Yodyunyong, S. Keipert-Colberg, Y. Botchak Mouafi, D. Borchert, and A. Montesdeoca-Santana, “Improvement of multicrystalline silicon solar cells by a low temperature anneal after emitter diffusion,” *Progress in Photovoltaics: Research and Applications*, vol. 19, pp. 165 – 169, 03 2011.
- [17] T. Niewelt, A. Richter, T. Kho, N. Grant, R. Bonilla, B. Steinhauser, J.-I. Polzin, F. Feldmann, M. Hermle, J. Murphy, S. Phang, W. Kwapil, and M. Schubert, “Taking monocrystalline silicon to the ultimate lifetime limit,” *Solar Energy Materials and Solar Cells*, vol. 185, pp. 252 – 259, 2018.
- [18] S. Gatz, K. Bothe, J. Müller, T. Dullweber, and R. Brendel, “Analysis of local al-doped back surface fields for high efficiency screen-printed solar cells,” *Energy Procedia*, vol. 8, pp. 318 – 323, 2011. Proceedings of the SiliconPV 2011 Conference (1st International Conference on Crystalline Silicon Photovoltaics).